Title

Matrix Mimetic Hydrogels for High-Throughput Screening

Author

Liang, Jesse

Publication Date

2022

Peer reviewed|Thesis/dissertation

UNIVERSITY OF CALIFORNIA

Los Angeles

Matrix Mimetic Hydrogels for High-Throughput Screening

A dissertation submitted in partial satisfaction of the

requirements for the degree Doctor of Philosophy

in Bioengineering

by

Jesse Liang

2022

ABSTRACT OF THE DISSERTATION

Matrix Mimetic Hydrogels for High Throughput Screening

by

Jesse Liang

Doctor of Philosophy in Bioengineering

University of California, Los Angeles, 2022

Professor Stephanie Kristin Seidlits, Chair

Cell-matrix interactions mediate complex physiological processes through biochemical, mechanical, and geometrical cues, influencing pathological changes and therapeutic responses. Accounting for matrix effects earlier in the drug development pipeline is expected to increase the likelihood of clinical success of novel therapeutics. Biomaterial-based strategies recapitulating specific tissue microenvironments in 3D cell culture exist but integrating these with the 2D culture methods primarily used for drug screening has been challenging. The development of methods which can incorporate the flexibility and utility of biomaterials will improve therapeutic development for diseases like Glioblastoma (GBM). Whose unique physiological characteristics have rendered traditional therapies ineffective for treatment. First, I adapt previous hydrogel-based technologies to be compatible with high-throughput (HT) drug screening platforms. Second, I further improve upon the underlying technique by developing a system capable of HT

screening of 3-dimensional cultures and demonstrate a proof-of concept personalized medicine type application. Third, I developed techniques to quantify and characterize the diffusivity of solutes into hydrogels to understand how physical pore size of hydrogels may affect penetration of therapeutics to encapsulated cells. Altogether, this work demonstrated the utility of including hydrogel-based technologies in screening platforms for drug development and the establishment of fundamental techniques to characterize the effectiveness of future therapeutics for GBM.

The dissertation of Jesse Liang is approved.

Benjamin M. Wu

Bennet G. Novitch

Song Li

Stephanie Kristin Seidlits, Committee Chair

University of California Los Angeles

2022

DEDICATION

I dedicate this work to my family, friends, and teachers who through my lifetime have supported me in my academic pursuits.

To my grandfather. Thank you for the tremendous courage, selflessness, and wisdom. You envisioned a better life for your family and took the steps to see it happen, our family will never forget your sacrifice.

To my father. Your time was short, but your impact immeasurable. Thank you for your example and wisdom. I hope I would have made you proud.

To my mother. No number of words can capture the depth of sacrifice and love you have poured out. Thank you.

To my wife, the most patient, and loving partner I do not deserve. Thank you for believing in me when I didn’t believe in myself.

TABLE OF CONTENTS

Contents

TABLE OF FIGURES

ACKNOWLEDGMENTS

Chapter 2 is adapted from: Liang, J., Sohrabi, A., Epperson, M., Rad, L. M., Tamura, K., Sathialingam, M., Skandakumar, T., Lue, P., Huang, J., Popoli, J., Yackly, A., Bick, M., Wang, Z. Z., Chen, C. C., Varuzhanyan, G., Damoiseaux, R., Seidlits, S. K. Hydrogel Arrays Enable Increased Throughput for Screening Effects of Matrix Components and Therapeutics in 3D Tumor Models. J. Vis. Exp. (Pending Publication), e63791, In-press (2022).

VITA

Education

University of California, Los Angeles

B.S. Bioengineering 2010-2014

Research Appointments

Graduate Student Researcher, University of California, Los Angeles 2014-2020

Professor Stephanie Seidlits, Department of Bioengineering

Undergraduate Student Researcher, University of California, Los Angeles 2011-2014

Professor Benjamin Wu, Department of Bioengineering

High School Research Intern, University of California, San Diego 2010

Professor Dwayne Stupack, Department of Pathology

Teaching Portfolio

BE176 – Biocompatibility 2019

Teaching Assistant, Guest Lecturer

BE180 – System Integration of Biology, Engineering, and Medicine I 2019

Teaching Assistant, Guest Lecturer

BE167L – Bioengineering Laboratory 2015, 2016, 2018

Head Teaching Assistant, and Section Teaching Assistant, Guest Lecturer

Grants/Awards/Honors

SLAS Tony B. Academic Travel Award 2019

University Fellowship (Bioengineering Department) 2018, 2019

NIH T32 Fellowship, Genomic Apprentice Teaching Program 2016 - 2018

UC Systemwide Bioengineering Symposium: Podium Presentation Award 2017

UCLA OID IIP award, *Proposal for Improvements to BE167L: Introduction to Bioengineering Laboratory Course* (contributing author) 2016

Selected Publications

Seidlits SK, **Liang J**, Bierman RD, Sohrabi A, Karam J, Holley SM, Cepeda C, Walthers CM. Peptide-modified, hyaluronic acid-based hydrogels as a 3D culture platform for neural stem/progenitor cell engineering. J Biomed Mater Res A. 2019 Apr;107(4):704-718. doi: 10.1002/jbm.a.36603. Epub 2019 Jan 21. PubMed PMID: 30615255.

Ballard ZS, Joung HA, Goncharov A, **Liang J**, Nugroho K, Di Carlo D, Garner OB, Ozcan A. Deep learning-enabled point-of-care sensing using multiplexed paper-based sensors. NPJ Digit Med. 2020;3:66. doi: 10.1038/s41746-020-0274-y. eCollection 2020. PubMed PMID: 32411827; PubMed Central PMCID: PMC7206101.

Xiao W, Zhang R, Sohrabi A, Ehsanipour A, Sun S, **Liang J**, Walthers CM, Ta L, Nathanson DA, Seidlits SK. Brain-Mimetic 3D Culture Platforms Allow Investigation of Cooperative Effects of Extracellular Matrix Features on Therapeutic Resistance in Glioblastoma. Cancer Res. 2018 Mar 1;78(5):1358-1370. doi: 10.1158/0008-5472.CAN-17-2429. Epub 2017 Dec 27. PubMed PMID: 29282221; PubMed Central PMCID: PMC5935550.

Xiao W, Wang S, Zhang R, Sohrabi A, Yu Q, Liu S, Ehsanipour A, **Liang J**, Bierman RD, Nathanson DA, Seidlits SK. Bioengineered scaffolds for 3D culture demonstrate extracellular matrix-mediated mechanisms of chemotherapy resistance in glioblastoma. Matrix Biol. 2020 Jan;85-86:128-146. doi: 10.1016/j.matbio.2019.04.003. Epub 2019 Apr 24. PubMed PMID: 31028838; PubMed Central PMCID: PMC6813884.

Chapter 1. Introduction to Glioblastoma

Glioblastoma (GBM) is the most common and uniformly lethal brain tumor, the overall survival newly diagnosed patients ranges from 13 – 19 months with the five year overall survival (OS) estimated at 6.8%.[1,2] The current survival rate is the result of an innovation in GBM management reported in 2005 and involves the maximal safe resection of the primary tumor, followed by radiotherapy and temozolomide.[3] The lack of advancement of therapies in the intervening years from 2005 until the present has not been for lack of effort. According to the NIH clinical trial website of the 1720 studies associated with the query "glioblastoma" none have been approved for marketing.[4] The overwhelming lethality of GBM in the face of state-of-the-art therapies is well known and is often attributed to its unique and complex biology.[5] Three features of GBM which contribute to these outcomes are its diffuse infiltrative nature (blunting the effectiveness of resection procedures), the chemoresistance of its cancer stem cell (CSC) population, and the cold or immunosuppressive tumor microenvironment (TME) of GBM.

1.1. GBM Therapeutics

Current standard of care for GBM includes resection of the primary tumor, followed by radiotherapy and temozolomide (TMZ).[3] During resection of the primary tumor advances in technologies which help discriminate the border of the tumor have significantly improved the outcomes of patients.[6] Beyond the removal of the primary tumor, radiotherapy regimens have also been used to help ablate the growth of residual tumor cells. Often, a chemotherapeutic regimen consisting of an alkylating agent such as TMZ is taken as well, and additional clinical trials are underway investigating the potential for other targeted therapeutics.[7]

TMZ is a small molecule alkylating agent which act by methylation of purine bases of DNA forming O6-methylguanine residues throughout the target DNA. [8]Upon oral administration, TMZ is readily absorbed and is broken down under physiological pH to monomethyl triazene which further reacts to form methyldiazomium cation which can form the O6-Meg lesions. If not repaired by cellular machinery, these modified guanines will incorrectly base pair and trigger the DNA mismatch repair enzyme, halting DNA synthesis and eventual apoptosis in an ATR-CHK1-dependent manner.[9] This mechanism of cytotoxicity depends on the absence of methylguanine-DNA methyltransferase (MGMT) enzyme which can reverse the alkylation by TMZ. Accordingly, methylation of the MGMT promoter is associated with better survival outcomes for patients.[10] Unfortunately, TMZ resistance inevitably emerges in GBM through a combination of natural resistance to apoptosis and intratumoral heterogeneity with a subset of cells eventually emerging that are ultimately resistant to TMZ treatment.[11]

As TMZ is commonly utilized as a general approach, other strategies to target GBM specifically through targeted inhibition of critical GBM pathways have also been tested in the clinic.[12] Molecular characterization of GBM has been the focus of many groups, including The Cancer Genome Atlas (TCGA_ which has broadly categorized GBM into a proneural, classical and mesenchymal subtypes through transcriptomic and genomic characterization of hundreds of patient samples.[13–15] Follow up work by other groups has revealed additional epigenetic signatures.[16,17] Nonetheless, these efforts to molecularly classify GBM have helped identify several targets that are highly upregulated in GBM and represent candidates whose disruption may promote targeted destruction of GBM. Unfortunately, trials to exploit specific targets with

clinical success have been largely unsuccessful. We will examine two of these cases to understand why predicted efficacy of these compounds was incorrect.

1.2. Case study 1: Erlotinib, targeted EGFR inhibitor

In theory, targeted disruption of crucial processes of tumor proliferation should result in specific ablation of tumor function and promote patient health. In many cancers including GBM, epidermal growth factor receptor (EGFR) is highly mutated and upregulated and becomes a central receptor whose activity helps promote tumor cell proliferation.[18,19] Targeted disruption of EGFR would thus provide a simple manner by which one can specifically target cancer-cell specific machinery to ablate cancer growth while leaving other cellular functions predominantly intact. Indeed, this strategy has been used to great success in other cancers such as breast cancer and melanoma where erlotinib as a targeted therapeutic was successful.[18]

In the case of GBM, however, treatment with erlotinib was found to be a disappointing failure, with clinical trials demonstrating little to no effect on reduction of tumor burden by treatment with erlotinib.[20] A postmortem analysis of this therapeutic revealed that while EGFR is indeed a major player in GBM physiology several other cellular mechanisms precluded the efficacy of erlotinib in targeting GBM. These factors include penetration of the drug across the blood brain barrier, efflux pump receptors, as well as constitutively active EGFR isoforms which preclude the effectiveness of erlotinib.[21,22] Additionally, cellular heterogeneity within GBM tumors, wherein differential expression of EGFR, and dependence, preclude the effectiveness of targeted strategies like EGFR.[23,24] Furthermore, in cells which are reliant on GBM synergistic signaling through the physical microenvironment provides routes for GBM to escape targeted knockdown of EGFR. [19] As a result, future successful therapies including targeted inhibition must be

combined with additional therapeutics to prevent the acquisition of drug resistance through escape pathways.

Following surgical and radiological methods to remove and weaken the tumor, GBM therapies then turn to the utilization of drugs and biologics to control the residual tumor cells. The general strategy of drugs, erlotinib and cilengitide, and biologics, monoclonal antibodies to overexpressed tumor protein (e.g., EGFR), is the targeted disruption of internal cellular processes which either diminish the viability of the tumor or its invasiveness, and in the case of antibody-based therapies initiate antibody-mediated cytotoxicity.

1.3. Case Study 2: Cilengitide, targeted integrin inhibitor

Beyond drug resistance, another critical biological behavior of GBM contributing to its overtly lethal profile is its diffuse migratory nature. Individual cells can migrate as far as 200 μm from the bulk tumor and commonly can be seen to be migrating via white matter tracts or even blood vessels.[25]Another successful tool in the clinic for treatment of other cancers with migratory and/or metastatic behaviors was the drug cilengitide, a cyclic RGD peptide which targets to the extracellular matrix (ECM) binding motif of integrins thereby discouraging integrin mediated mobility of tumor cells.[26] Again, cyclo-RGD ended as a disappointing failure in the clinic with no significant survival gains by the patient.[27] One explanation for these disappointing results is the ECM composition in the brain, which features predominantly a sugar-based network with very little if any fibrous collagen and other proteins.[28] Furthermore, the sugar-based network containing a relatively high abundance of hyaluronic acid (HA) has gained significant traction, representing an axis for signaling by both physical and biochemical means to regulate and promote many of the aggressive behaviors of GBM.[29–32]

In two case studies, we note that the *in vitro* studies suggesting critical roles for EGFR signaling and integrin based signaling in the progression of GBM was not incorrect.[33–37] Rather, the effectiveness of targeting these players was greatly diminished by effects provided by HA rich matrix. Indeed, the role of HA in both the progression of and biology of GBM has been the matter of focus for many years. [38] For these reasons, we will now primarily consider the effects of HA in GBM biology.

Hyaluronic acid (HA) is a nonsulfated glycosylated aminoglycan that forms the structural basis of central nervous system (CNS) ECM.[39,40] HA is known to induce cellular signaling through binding to its main extracellular receptor CD44 as well as its other known binding receptor CD168.[41] Beyond signaling through its primary receptor, HA has been shown to dimerize with other extracellular receptors including integrins, EGFR, Toll like receptors, as well as others[42–44]. Following binding and clustering of these extracellular receptors intracellularly HA based signals through signaling cascades, MAPK, and PI3K, as well as through cytoskeletal components through proteins such as Ezrin.[44–47]

HA extracellular concentration is regulated through the coordinated activity of HA synthases and hyaluronidases, such that cell responses to HA can be binned in either a high molecular weight, or low molecular weight mode.[48] The cleavage of HA from high molecular weight to low molecular weight is accomplished by hyaluronidase enzymes, which can be localized either intracellularly or extracellularly.[49] Besides hyaluronidases, HA molecular weight is also controlled by factors in the microenvironment including oxidative activity mediated by

macrophages, microglia, and astrocytes.[50,51] Particularly in inflammatory environments, HA is known to be degraded and potentiate the inflammatory response as identified in several neurological disorders, including multiple sclerosis, traumatic brain injury, and spinal cord injury.[52,53] This is in contrast to normal tissue where intact high HA molecular weight is believed to play important roles in maintaining an anti-inflammatory microenvironment.[54]

In GBM specific contexts, HA has been shown to participate in various signaling pathways to promote both migration and drug resistance. [29,32,55–59] These studies were done by leveraging biomaterial approaches to recapitulate aspects of the GBM TME through HA-based hydrogels.[29,55] As noted from the above case studies, presentation of the ECM cues via hydrogels can serve as effective surrogates for *ex vivo* modelling of GBM tumors. This dissertation focuses on the development of methodologies to adapt these biomaterials for use in therapeutic development.

In chapter 2, I demonstrate how tissue engineering principles were used to develop an HA-hydrogel based platform to improve drug screening of GBM through increasing the throughput of hydrogel generation. In chapter 3, I extend these methods to three-dimensional formats and demonstrate a proof-of-concept matrix screening approach on patient derived GBM cells. Finally in chapter 4, I demonstrate how matrix properties affect diffusivity and partitioning of solutes and discuss the implication of those studies on emerging GBM therapeutics.

1.4. References

1. Ostrom, Q. T., Cioffi, G., Waite, K., Kruchko, C. & Barnholtz-Sloan, J. S. CBTRUS Statistical Report: Primary Brain and Other Central Nervous System Tumors Diagnosed in the United States in 2014–2018. *Neuro-Oncology* **23**, iii1–iii105 (2021).

2. Feng, E., Sui, C., Wang, T. & Sun, G. Temozolomide with or without Radiotherapy in Patients with Newly Diagnosed Glioblastoma Multiforme: A Meta-Analysis. *European Neurology* **77**, 201–210 (2017).

3. Stupp, R. *et al.* Radiotherapy plus Concomitant and Adjuvant Temozolomide for Glioblastoma. *New England Journal of Medicine* **352**, 987–996 (2005).

4. Home - ClinicalTrials.gov. https://clinicaltrials.gov/.

5. Cosset, É., Weis, S. M. & Cheresh, D. A. Re-thinking the preclinical development of GBM therapeutics. *Oncoscience* **5**, 11–12 (2018).

6. Chohan, M. O. & Berger, M. S. 5-Aminolevulinic acid fluorescence guided surgery for recurrent high-grade gliomas. *J Neurooncol* **141**, 517–522 (2019).

7. Sharma, P. & Debinski, W. Receptor-targeted glial brain tumor therapies. *International Journal of Molecular Sciences* **19**, (2018).

8. Herbener, V. J. *et al.* Considering the experimental use of Temozolomide in glioblastoma research. *Biomedicines* **8**, 1–29 (2020).

9. Zhang, J., F.G. Stevens, M. & D. Bradshaw, T. Temozolomide: Mechanisms of Action, Repair and Resistance. *Current Molecular Pharmacology* **5**, 102–114 (2012).

10. Zhang, J., F.G. Stevens, M. & D. Bradshaw, T. Temozolomide: Mechanisms of Action, Repair and Resistance. *Current Molecular Pharmacology* **5**, 102–114 (2012).

11. Lee, S. Y. Temozolomide resistance in glioblastoma multiforme. *Genes and Diseases* vol. 3 198–210 (2016).

12. Su, J. *et al.* Molecularly Targeted Drugs Plus Radiotherapy and Temozolomide Treatment for Newly Diagnosed Glioblastoma: A Meta-Analysis and Systematic Review. *Oncology Research Featuring Preclinical and Clinical Cancer Therapeutics* **24**, 117–128 (2016).

13. Verhaak, R. G. W. *et al.* Integrated genomic analysis identifies clinically relevant subtypes of glioblastoma characterized by abnormalities in PDGFRA, IDH1, EGFR, and NF1. *Cancer Cell* **17**, 98–110 (2010).

14. Tomczak, K., Czerwińska, P. & Wiznerowicz, M. The Cancer Genome Atlas (TCGA): an immeasurable source of knowledge. *Contemporary oncology (Poznan, Poland)* **19**, A68–A77 (2015).

15. Brennan, C. W. *et al.* The somatic genomic landscape of glioblastoma. *Cell* **155**, 462–477 (2013).

16. Yu, W. *et al.* Construction of Novel Methylation-Driven Gene Model and Investigation of PARVB Function in Glioblastoma. *Front Oncol* **11**, (2021).

17. Cong, P. *et al.* Identification of the Role and Clinical Prognostic Value of Target Genes of m6A RNA Methylation Regulators in Glioma. *Front Cell Dev Biol* **9**, (2021).

18. Ueno, N. T. & Zhang, D. Targeting EGFR in triple negative breast cancer. *J Cancer* (2011) doi:10.7150/jca.2.324.

19. Pedron, S., Hanselman, J. S., Schroeder, M. A., Sarkaria, J. N. & Harley, B. A. C. Extracellular Hyaluronic Acid Influences the Efficacy of EGFR Tyrosine Kinase Inhibitors in a Biomaterial Model of Glioblastoma. *Advanced Healthcare Materials* **6**, 1700529 (2017).

20. Brown, P. D. *et al.* Phase I/II Trial of Erlotinib and Temozolomide With Radiation Therapy in the Treatment of Newly Diagnosed Glioblastoma Multiforme: North Central Cancer Treatment Group Study N0177. *Journal of Clinical Oncology* **26**, 5603 (2008).

21. Biernat, W., Huang, H., Yokoo, H., Kleihues, P. & Ohgaki, H. Predominant expression of mutant EGFR (EGFRvIII) is rare in primary glioblastomas. *Brain Pathol* **14**, 131–136 (2004).

22. Heimberger, A. B., Suki, D., Yang, D., Shi, W. & Aldape, K. The natural history of EGFR and EGFRvIII in glioblastoma patients. *Journal of Translational Medicine* **3**, 1–6 (2005).

23. Bonavia, R. *et al.* EGFRvIII promotes glioma angiogenesis and growth through the NF-κB, interleukin-8 pathway. *Oncogene 2012 31:36* **31**, 4054–4066 (2011).

24. Heimberger, A. B. *et al.* Prognostic effect of epidermal growth factor receptor and EGFRvIII in glioblastoma multiforme patients. *Clin Cancer Res* **11**, 1462–1466 (2005).

25. Claes, A., Idema, A. J. & Wesseling, P. Diffuse glioma growth: A guerilla war. *Acta Neuropathologica* **114**, 443–458 (2007).

26. Burke, P. A. *et al.* Cilengitide targeting of alpha(v)beta(3) integrin receptor synergizes with radioimmunotherapy to increase efficacy and apoptosis in breast cancer xenografts. *Cancer Res* **62**, 4263–4272 (2002).

27. Scaringi, C., Minniti, G., Caporello, P. & Enrici, R. M. Integrin inhibitor cilengitide for the treatment of glioblastoma: A brief overview of current clinical results. *Anticancer Research* **32**, 4213–4224 (2012).

28. The role of extracellular matrix in CNS regeneration. *Current Opinion in Neurobiology* **17**, 120–127 (2007).

29. Pedron, S. *et al.* Hyaluronic acid-functionalized gelatin hydrogels reveal extracellular matrix signals temper the efficacy of erlotinib against patient-derived glioblastoma specimens. *Biomaterials* **219**, 119371 (2019).

30. Kim, Y. & Kumar, S. CD44-mediated Adhesion to Hyaluronic Acid Contributes to Mechanosensing and Invasive Motility. *Mol Cancer Res* **12**, 1416 (2014).

31. Kim, Y. & Kumar, S. CD44-Mediated Adhesion to Hyaluronic Acid Contributes to Mechanosensing and Invasive Motility. *Molecular Cancer Research* **12**, 1416–1429 (2014).

32. Chen, J. W. E. *et al.* Influence of Hyaluronic Acid Transitions in Tumor Microenvironment on Glioblastoma Malignancy and Invasive Behavior. *Front Mater* **5**, (2018).

33. Guillamo, J. S. *et al.* Molecular mechanisms underlying effects of epidermal growth factor receptor inhibition on invasion, proliferation, and angiogenesis in experimental glioma. *Clinical Cancer Research* **15**, 3697–3704 (2009).

34. Reardon, D. A., Nabors, L. B., Stupp, R. & Mikkelsen, T. Cilengitide: An integrin-targeting arginine-glycine-aspartic acid peptide with promising activity for glioblastoma multiforme. *Expert Opinion on Investigational Drugs* **17**, 1225–1235 (2008).

35. Stupp, R. *et al.* Phase I/IIa study of cilengitide and temozolomide with concomitant radiotherapy followed by cilengitide and temozolomide maintenance therapy in patients with newly diagnosed glioblastoma. *Journal of Clinical Oncology* **28**, 2712–2718 (2010).

36. Rude Voldborg, B., Damstrup, L., Spang-Thomsen, M. & Skovgaard Poulsen, H. Epidermal growth factor receptor (EGFR) and EGFR mutations, function and possible role in clinical trials. *Annals of Oncology* **8**, 1197–1206 (1997).

37. Fukai, J., Nishio, K., Itakura, T. & Koizumi, F. Antitumor activity of cetuximab against malignant glioma cells overexpressing EGFR deletion mutant variant III. *Cancer Science* **99**, 2062–2069 (2008).

38. Xiao, W., Sohrabi, A. & Seidlits, S. K. Integrating the glioblastoma microenvironment into engineered experimental models. *Future Sci OA* **3**, FSO189 (2017).

39. CD44 isoforms during differentiation and development. *BioEssays* **17**, 17–24 (1995).

40. Mechanism and biological significance of CD44 cleavage. *Cancer Science* **95**, 930–935 (2004).

41. CD44: From adhesion molecules to signalling regulators. *Nature Reviews Molecular Cell Biology* **4**, 33–45 (2003).

42. CD44: From adhesion molecules to signalling regulators. *Nature Reviews Molecular Cell Biology* **4**, 33–45 (2003).

43. CD44: A Multifunctional Cell Surface Adhesion Receptor Is a Regulator of Progression and Metastasis of Cancer Cells. *Frontiers in Cell and Developmental Biology* **5**, (2017).

44. The role of the CD44 transmembrane and cytoplasmic domains in co-ordinating adhesive and signalling events. *Journal of Cell Science* **117**, 373–380 (2004).

45. Signaling through CD44 Is Mediated by Tyrosine Kinases ASSOCIATION WITH p56lck IN T LYMPHOCYTES. *Journal of Biological Chemistry* **271**, 2863–2867 (1996).

46. Dynamic changes of CD44 expression from progenitors to subpopulations of astrocytes and neurons in developing cerebellum. *PloS One* **8**, e53109 (2013).

47. Berneau, S. C. *et al.* Investigating the role of CD44 and hyaluronate in embryo-epithelial interaction using an in vitro model. *MHR: Basic science of reproductive medicine* **25**, 265–273 (2019).

48. Hyaluronic Acid in Inflammation and Tissue Regeneration. https://www.hmpgloballearningnetwork.com/site/wounds/article/hyaluronic-acid-inflammation-and-tissue-regeneration.

49. The magic glue hyaluronan and its eraser hyaluronidase: A biological overview. *Life Sciences* **80**, 1921–1943 (2007).

50. Vistejnova, L. *et al.* Low molecular weight hyaluronan mediated CD44 dependent induction of IL-6 and chemokines in human dermal fibroblasts potentiates innate immune response. *Cytokine* **70**, 97–103 (2014).

51. Fuchs, K. *et al.* Opposing effects of high-and low-molecular weight hyaluronan on CXCL12-induced CXCR4 signaling depend on CD44. *Cell Death and Disease* **4**, (2013).

52. Struve, J. *et al.* Disruption of the hyaluronan-based extracellular matrix in spinal cord promotes astrocyte proliferation. *GLIA* **52**, 16–24 (2005).

53. Diao, S., Xiao, M. & Chen, C. The role of hyaluronan in myelination and remyelination after white matter injury. *Brain Res* **1766**, (2021).

54. Molecular weight and concentration of heparin in hyaluronic acid-based matrices modulates growth factor retention kinetics and stem cell fate. *Journal of Controlled Release: Official Journal of the Controlled Release Society* **209**, 308–316 (2015).

55. Xiao, W., Ehsanipour, A., Sohrabi, A. & Seidlits, S. K. Hyaluronic-Acid Based Hydrogels for 3-Dimensional Culture of Patient-Derived Glioblastoma Cells. *JoVE (Journal of Visualized Experiments)* **2018**, e58176 (2018).

56. Yu, Q. *et al.* Extracellular Matrix Proteins Confer Cell Adhesion-Mediated Drug Resistance Through Integrin α v in Glioblastoma Cells. *Front Cell Dev Biol* **9**, (2021).

57. Xiao, W. *et al.* Brain-mimetic 3D culture platforms allow investigation of cooperative effects of extracellular matrix features on therapeutic resistance in glioblastoma. *Cancer Research* **78**, 1358–1370 (2018).

58. Chen, Dr. J.-W. E., Leary, Mr. S., Barnhouse4, Mr. V., Sarkaria, Dr. J. N. & Harley, Dr. B. A. C. Matrix hyaluronic acid and hypoxia influence a CD133+ subset of patient-derived glioblastoma cells. *https://home.liebertpub.com/tea* (2021) doi:10.1089/TEN.TEA.2021.0117.

59. Ghochani, Y. *et al.* Generation of a molecular interactome of the glioblastoma perivascular niche reveals Integrin Binding Sialoprotein as a key mediator of tumor cell migration. *bioRxiv* 2021.10.01.462643 (2021) doi:10.1101/2021.10.01.462643.

Chapter 2. Imaging Based Screening Approaches Reveal Biomimetic Peptide Effects on GBM Drug Resistance

2.1. Introduction

Glioblastoma (GBM) is the most common and highly lethal cancer to arise from central nervous system tissue with an estimated survival rate of 6.8 % of patients five years post diagnosis from the period of 2014-2018.[1] Poor patient outcomes occur despite an aggressive treatment regimen of maximal safe surgical resection of the primary tumor and concomitant radiotherapy and chemotherapy (Stupp Protocol). [2] The failure of this treatment regimen can be attributed to two widely known attributes of GBM. First, its diffuse invasion into surrounding brain tissue, makes complete resection, despite advances in methods to illuminate the tumor border, impossible.[3] Secondly, the cancer stem cell (CSC) compartment of the GBM tumor demonstrates strong chemotherapeutic resistance and is also known to demonstrate increased aggressiveness when exposed to radiotherapy.[4] The lack of effective treatment strategies draws attention to the dire need to develop novel effective therapeutics.

Many different modalities of GBM therapeutics are in development, including small molecule drugs, biologics, immunotherapies, cell, and gene therapies, as well as medical devices.[5] The current standard of radiotherapy and adjuvant temozolomide (TMZ) falls under the realm of small molecule drugs and we will focus on that classification of drug as the regulatory and manufacturing pathways for these molecules is the most well developed.[6]

In standard drug screening workflows, 2D cultured GBM cells, such as U87, are exposed to compound libraries numbering in the tens of thousands and screened for effects at the population level. These processes have been finely honed for speed and reproducibility, including built-in

statistical measures of success, allowing for the identification of promising compounds to be taken further down the drug development pipeline.[7] One critique of these standard methods has been the lack of tumor microenvironment namely the blood-brain barrier (BBB) and physical ECM creates an artificial environment with weaknesses in the cultured cells that is not representative of the parent tumor. In recent years, an increased focus on GBM biology has revealed GBM's dependence on its local tumor microenvironment (TME) to be a major driver of its biological characteristics. GBMs interaction with the physical extracellular matrix (ECM) has been linked to its resistance to treatment by temozolomide.[5,8] The GBM TME features an abundance of hyaluronic acid which via its cellular receptors (CD44, CD168) has been implicated in mediating acquisition of drug resistance to TMZ. [9]

A recent innovation in drug screening assays has been the usage of gliomaspheres which are three dimensional aggregate cultures which synthesize their own ECM and are believed to be more physiologically relevant.[10] Despite these advances we and others have shown that further recapitulation of aspects of the native TME, such as provision of an hyaluronic acid (HA) based matrix, is able to grant *in vitro* cultures of GBM cells increased resistance to therapeutics that would previously have been predicted to be effective against GBM.[11–16]

Unfortunately, the addition of these HA based matrices comes at the cost of throughput thereby slowing adoption of these methods into traditional drug screening platforms. A major barrier to adoption of these technologies lies in the fact that the protocols for fabrication of these novel matrices are not compatible with high-throughput screening workflows.[17] Indeed, this lack of compatibility is evident when one considers that many of these approaches were not designed with the throughput of traditional drug screening libraries in mind. Furthermore, the flexibility of

hydrogel-based technologies also presents a challenge to end users as the selection of the 'optimal' characteristics of the hydrogel system is non-trivial.[18] Thus, in addition to methods to manufacture hydrogels in high throughput, methods which enable the rational selection of relevant features, hydrogel stiffness, composition, ligand presentation, is also necessary.[19] Another weakness of the traditional methodology for drug screening is the population-level readout typically performed to assess efficacy.[20] The recent boom in single-cell biology spearheaded by methods such as single cell RNA sequencing has revealed the extent of heterogeneity within a GBM tumor.[21] Thus, with the capability to screen at single cell resolution are expected to yield the greatest insight into GBM biology. Indeed, it is suspected that by increasing the resolution of screening to that of single cells is expected to yield highly valuable information of vulnerabilities of subpopulations within the bulk populations.[22]

Intratumoral heterogeneity represents a significant barrier to therapeutic development as the rich diversity of cell and cellular subtypes may mitigate effectiveness of therapeutics.[4,23] Developing methods which allow for the quantification of cellular response at the single-cell level will lead to characterization of this heterogeneity and, subsequently, improved therapeutic development. In this chapter I will discuss my efforts to advance GBM drug screening by developing methods by adapting previously developed HA based hydrogel technology into a high throughput (HT) compatible format. Furthermore, we also develop the capacity to perform matrix screening and an example workflow to select an 'optimized' matrix condition which maximizes drug resistance for a given cell type. We enable these features while simultaneously expanding the resolution of measurements by adopting an imaging-based readout in anticipation of the importance of single cell readouts. In our previous studies, we demonstrated how the provision of a HA-rich hydrogel

environment granted GBM cultures increased resistance to TMZ in an SRC dependent manner.[24,25] We report our efforts to adapt our tissue-engineered, ECM-GBM interface to a format compatible with traditional drug screening methods. Our platform leverages the strength of tissue engineering approaches to modulate cellular function and combines it with the speed and precision of high-throughput workflows. Increased throughput and deposition of cell-laden hydrogel samples is accomplished through a microfluidic chip liquid handler the Mantis (Formulatrix). While daily imaging to capture the number of cells (Nuclear reporter protein) and their cell cycle state (FastFUCCI) was accomplished using a high content well-plate imager the ImageExpress XL. Analysis of data is performed using CellProfiler an open source python based image analysis software thereby expanding the utility of these approaches to others. [26] While we do not fully explore the capability of single cell phenotypic screening in our experiments, our workflow details the methods and considerations one must take in designing an experiment of this scale.

2.2. Materials and Methods

Preparation of hydrogel precursor solutions

Hydrogel precursor solutions were prepared as described previously.[27] In brief, thiolated hyaluronic acid (4-6% modification of carboxylic group, HA-SH) was dissolved in 20 mM HEPES-HBSS at 12.5 mg/mL (1.25 weight percent) along with 4-arm thiol terminated polyethylene glycol (PEG-SH) at a concentration to contribute the same number of thiol groups as HA-SH henceforth referred to as solution 1. Solution 2 was prepared by dissolving 4-Arm vinyl sulfone terminated PEG (PEG-VS) at a concentration such that a molar ratio of 1 SH:1.2 VS would be achieved by mixing solution 1 and solution 2 at a 1:1 ratio. Peptides from derived

from various peptides known to be upregulated in the GBM TME were added either alone or as pairs to achieve a final concentration of peptide of 270 μM in 20mM HEPES-HBSS.[28]

Mantis Dispensing Procedures

Gel solution, with and without cells, was loaded via pipette tip into low volume mantis chips and dispensed into various multiwell plates (96, 384, 1536). To assess dispensing precision 500 nl of PBS were dispensed into the center of each well using the manufacturers engineering drawing of well plates for reference. For hydrogel deposition, gel solution was dispensed after mixing and modifying dispense parameters to account for the increased viscosity of the gel solution. Crosslinking of dispensed polymer was accomplished by placing the plate inside an incubator (37 degrees Celsius) for 15 minutes then removed and media was added to each well. Verification of gel placement and visualization of encapsulated cells was performed with a bench top transillumination microscope.

Microscopy based Imaging Workflows

Cultures were imaged approximately every 24 hours using an ImageXpress XL at 37 degrees C and 5% CO2. Imaging was done on a 10X objective on transmitted light, FITC, Cy3, and Cy5 channels using the autofocus program within the imaging software. Custom fields of view were defined such that the entire droplet was captured via imaging. The autofocus algorithm was set to identify the bottom of the plate (via IR laser) and then displace the thickness of the bottom of the well plate.

Cell Culture

Patient derived GBM cultures (GS122 and GS304) were maintained in DMEM/F12 with Heparin (25 mg/mL), FGF2 (20 ng/mL), EGF 2 (50 ng/mL), Gem21 (b27 substitute) and normoicin (1x).

Media was refreshed for suspension cultures every 3 days until spheres reached a size of ~ 150 µm at which point they were passaged.[14] GBM Cell line U87 was maintained in DMEM supplemented with 10% fetal bovine serum and 1% antibiotic and antimycotic.

Cell passaging of spheroid was performed by incubation with accutase followed by manual pipetting to achieve a single cell suspension. Cells were passaged every 5- 7 days depending on cell line.

Lentiviral infection of GBM lines

Following passage, GBM lines were plated onto laminin coated wells and allowed to attach for 24 hours. Viral particles, for both FASTFUCCI and IRFP, were added at a ratio of 1 transducing unit per cell such that on average 2 transducing units, 1 FASTFUCCI and 1 IRFP, were added to each cell.

Temporal Cell Cycle monitoring

Deposited cultures were imaged every 24 hours in the same location over a period of 14 days with an imageexpress XL. All images were taken at 10X on 4 different filter sets brightfield, GFP, Cy3, and Cy7. Individual channel images were fed into a cell profiler pipeline to extract the numbers of nuclei along with their cell cycle state.

Drug Challenge

3 days after dispensing, cultures were challenged with Temozolomide (TMZ) in DMSO at 500µM in a 3 days on 3 days off format via half media changes at the start of each cycle. [14] Co-treatment with SRC inhibitor Dasatinib was performed by including Dasatinib at 100 nM in TMZ treated conditions. A Dasatinib only treatment was also obtained to verify marginal effects on cells.

Cellprofiler pipeline/segmentation

To determine the parameters for nuclei segmentation manual counts across several wells spanning the different conditions were used as a ground truth. Sweeps were performed across the varying parameter values for the functions in cell profiler until the automated quantification came within 10 percent of the manual counts. To assess generalizability, a separate set of images was quantified by the same pipeline and shown to come within the same parameters as above.

Statistical Analysis

Strictly standardized mean differences (SSMD) is a robust statistical measure of how likely a given treatment/condition performs in reference to a control and is commonly used in high throughput screening.[29] We use SSMD to rank the effect of various combinations of peptides to promote proliferation and drug resistance in a matrix screen of various peptides from proteins known to be upregulated in the GBM TME. [28]

2.3. Results

High-Throughput deposition of Hyaluronic Acid based Hydrogel in multiwell plates

To assess the feasibility of miniaturizing and adapting our HA-based technology to a multi-well plate platform we assessed the accuracy with which liquid handlers could dispense droplets of precursor solution into well plates using a liquid handler Mantis formulatrix. The Mantis is a microfluidic based liquid handler with low dead volumes, and a modular design with up to 6 independent cartridges for solution dispensing, making it ideal for our proof-of-concept studies. The high reaction speed of the thiol-malemide Michael like addition resulted in gelation of our polymer solutions upon mixing, thus we switched to a vinyl sulfone (VS) chemistry instead of the Michael addition chemistry utilized in our earlier studies (Figure 1A).[13] The lower reaction

speed of the thiol – VS Michael like addition allowed for the mixing of our two precursor solutions prior to dispensing in the Mantis.[30] Additionally, the VS chemistry allowed us to retain the ability to selectively display various GBM ECM derived peptides (Table 1) in a combinatorial manner.

We assessed the precision with which the Mantis was capable of depositing solution into multi well plates of sizes 96, 384, and 1536 wells. While the spacing of 1536 well plates were too tight to accommodate our experiments, the 96 and 384 well plate spacing was amenable to dispensing (Figure 1B/C). Initial tests with water droplets suggested excellent accuracy however, the increased viscosity of polymeric solutions required tuning of dispense settings. Specifically, the diaphragm pressure and vacuum for dispensing, and the timing interval of dispense were adjusted to increase accuracy of dispensed droplets. These alterations of parameters to allow for dispensing of polymeric solutions however increased the variability of misspots in 384 well plates due to static effects or wetting of the droplet to the walls of 384 well plates rendering significant portions of the plate unusable in an uncontrollable manner (Figure 1D). Deposition into 96 well plates were extremely consistent with no misspots and was the format of choice for the rest of the studies. Thus, 96 well plates were used for the rest of the study.

We benchmarked the deposition of HA-based hydrogels by comparing the time it took to prepare an equal number of gels (96) with our legacy methods. Including the 15-minute crosslinking time, deposition of gels following mixing of the 2 solutions took less than 20 minutes. For legacy methods, the process to complete the protocol as detailed in our previous publications could take up to two hours to complete. Additionally, the amount of hydrogel used in this new process is

approximately 160 times, further demonstrating cost savings and increase in throughput necessary for drug screening experiments.

Protein	Integrin-Binding Peptides	Peptide-Specific Integrins	Overexpressed ECM Receptors
Vitronectin	KGGPQVTRGDVFTMP	αv, β3	αv, α1, αv, α3, α5, α6, α7 α9, β1,β3, β4, β5, β8, CD44
Tenascin – C	RSTDLPGLKAATHYTITIRGV	α5, β1	
Integrin-binding sialoprotein	GGGNGEPRGDTYRAY	αv	
Osteopontin	TVDVPDGRGDSLAYG	αv, β1, β3, β5	
Fibronectin	GCGYGRGDSPG	αv, α5, β1, β3, β5, β8	

Table 2-1: Adhesive peptides derived from ECM in GBM Tumors, corresponding integrin receptors and pathologically overexpressed receptors in GBM

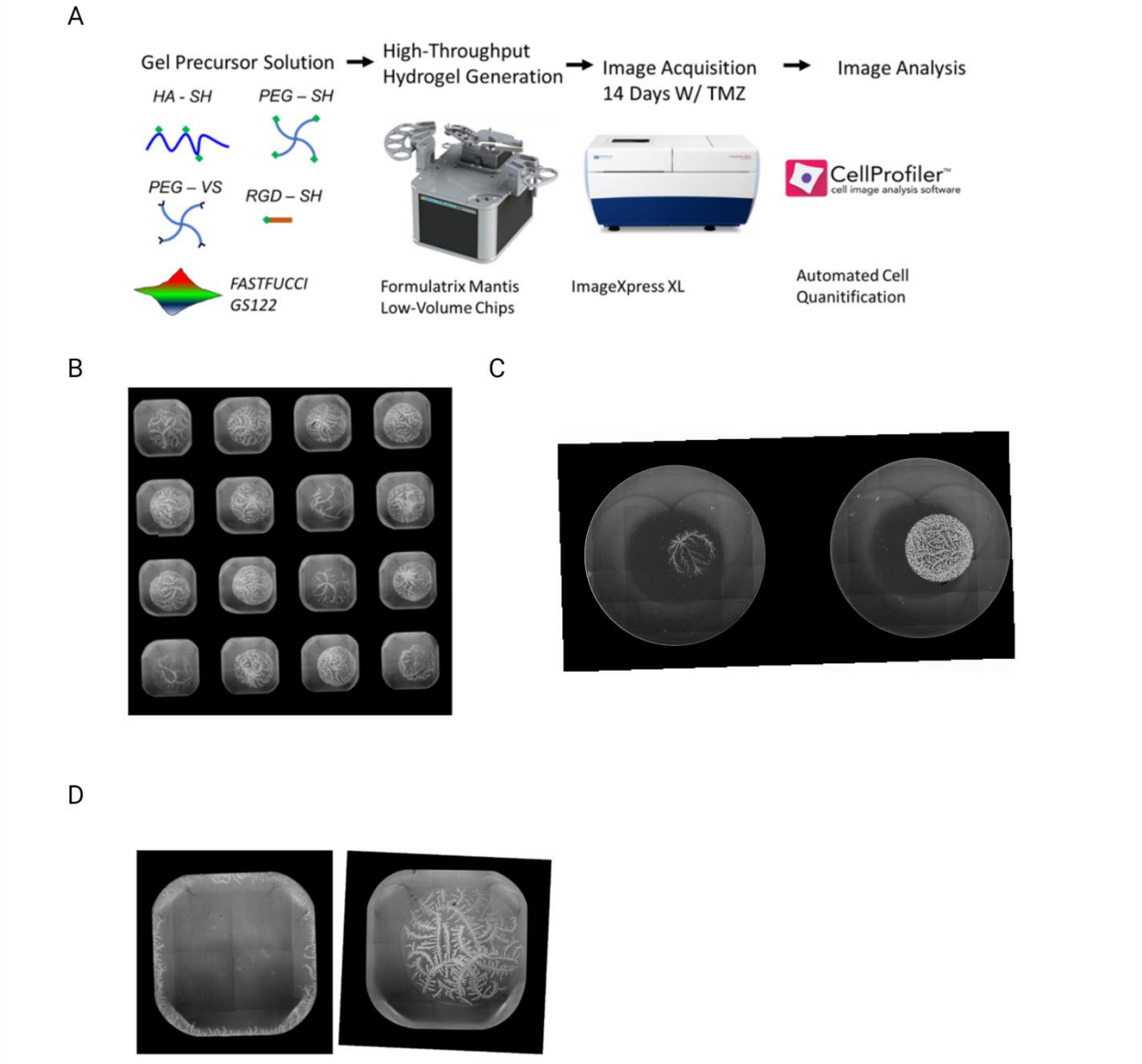

Figure 2-1: High Throughput Deposition of hydrogel into multiwell plates.
1A: Workflow overview. 1B: Verification of droplet dispense fidelity into 384 well plates. 1C: Verification of droplet dispense fidelity into 96 well plates. 1D: Example misspot (left) and proper spot (right)

Developing Methods for Longitudinal Imaging Based Studies

After validating the protocols for high throughput deposition of HA based hydrogels into a multiwell plate format, we then developed protocols for daily imaging of HA-gel augmented cultures. Standard drug screening is typically performed on the order of 24-48 hours following plating of compounds for 2D cultures. However, the kinetics of GBM drug resistance occurs on a longer time span ranging from weeks to months.[12] We utilized the capability of the Mantis to dispense 500 nanoliter volumes to seed a small portion of the well with cell laden cultures. This small initial seeding density allowed us to conduct our studies over a period of 15 days similar to our previous model. [14] In addition, we increased the resolution of our cell number characterization by leveraging the capabilities of the ImageXpress to perform daily imaging. This increase in sampling frequency garnered us higher resolution in resolving how our GBM cultures responded dynamically to a drug challenge. The protracted nature of our study also limited our ability to utilize exogenous stains for cell tracking, due to marker associated cytotoxicity as well as dilution effects. As TMZ is known to mediate its cytotoxicity through cell cycle arrest at the G2/M checkpoint we wanted required a reporter which tracked cell cycle state over the course of our study.[31] Additionally, accurate cell quantification is optimally achieved through the usage of nuclear localized dyes. To satisfy these requirements, we utilized an all in one variant of the fluorescence ubiquitination-based cell cycle indicator (FUCCI) reporter to track cell cycle and a histone 2b fusion protein to label the nuclei of our cultures.[32]

We assessed the feasibility of performing these long studies with 2 patient derived GBM cell lines (GS122 and GS304) as well as the transformed GBM cell line U87, commonly used for drug screening. Following lentiviral co-transduction of the two plasmids cells were expanded for two passages and then passaged for deposition into well plates. Lentivirally transduced cells expressed all proteins throughout the 15 days and proliferated in media verifying the cytocompatibility of our method (Figure 2A). To capture cell growth as a function of time images from each day over the entirety of area containing hydrogel droplets were quantified by cell profiler. Tuning of hyperparameters for the various modules used in cellProfiler to detect individual nuclei was done by manually counting a subset of images and identifying the combination of parameters which performed optimally (Figure 2B). Quantification of cell number over time in media conditions for both GS and gel augmented cultures also revealed an increase in cells undergoing cell cycling. (Figure 2C).

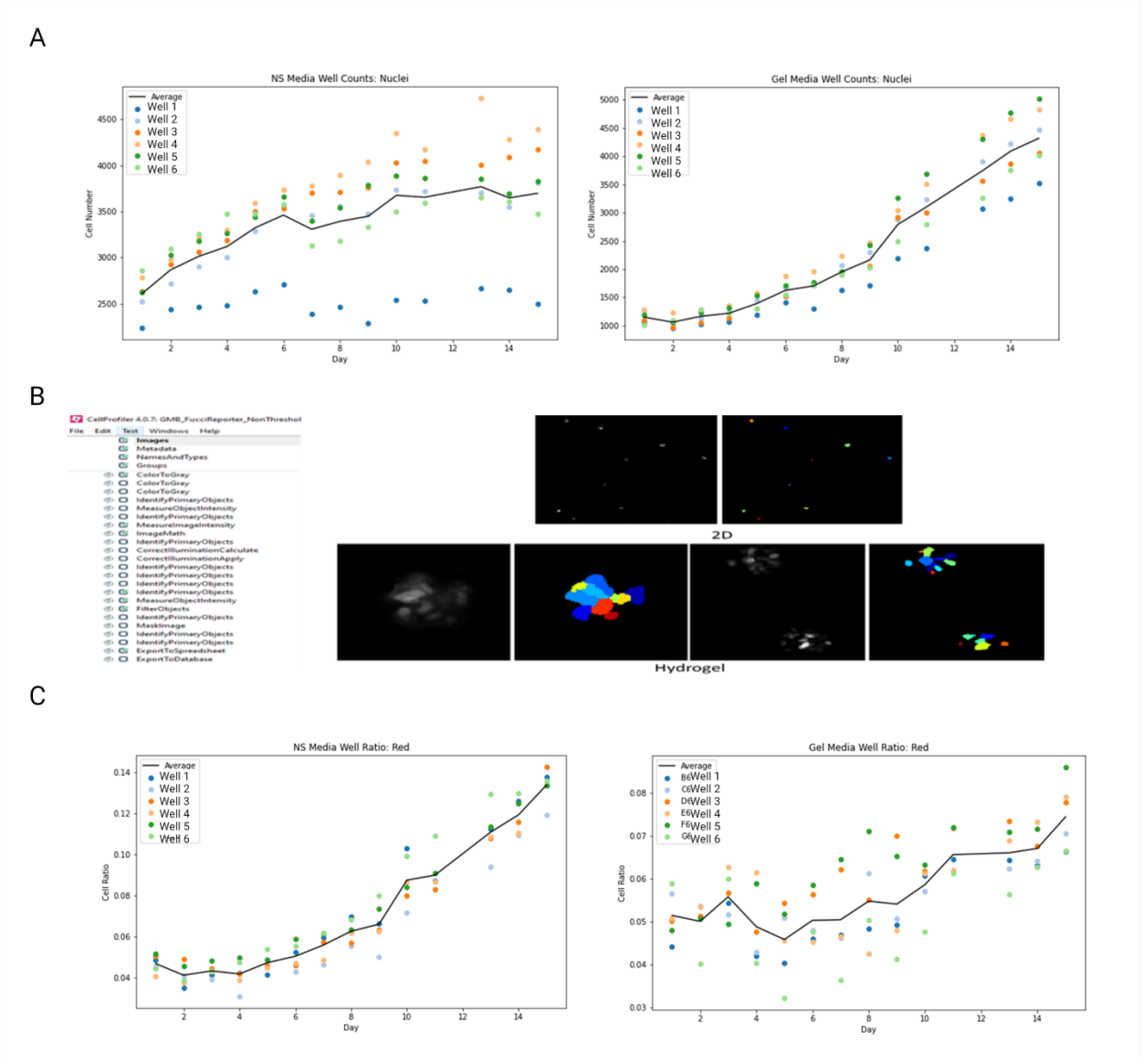

Figure 2-2: Validation of imaging workflow and quantification analyses.
2A: GS304 cells proliferate when deposited either as gel laden cultures or as single cell suspension over 15 days. Solid line = average of all wells 2B: Example of Cellprofiler pipeline for automated image analysis and segmentation of individual nuclei for counting of absolute cell number and cells in various stages of cell cycle. 2C: GS304 cells increase in the number of cells cycling over the course of the 15-day assay when cultured in media.

Evaluation of miniaturized HA gel platform to recapitulate drug resistance acquisition in GBM cultures

To qualify the utility of our method in a drug screening application we sought to replicate results we obtained from a previous report wherein patient derived GBM cell lines demonstrated resistance to alkylating agent temozolomide in a SRC dependent manner. In our previous report, we utilized a 3D culture platform in which the entire culture was surrounded by the HA matrix in a 3D format. As we observed robust spheroid formation in HA augmented cultures, we hypothesized that mechanisms like what we identified in our previous study would be at play in these cultures as well.[13,27] Towards that end we sought to evaluate if our miniaturized HA platform could provide the same benefits towards drug resistance as our previous culture model, but with the throughput of traditional 2D screening models. Unfortunately, we found that the GS122 line was more fragile than the GS304 line and did not tolerate cotransduction with our two lentiviruses. Thus, we were only able to assess how the provision of a hyaluronic acid-based matrix would affect GS304s under the context of a drug challenge with TMZ at 500 µM compared to gliomasphere conditions. Additionally, patient derived GBM cell lines GS122 and GS304 exhibited a large reduction in the expression of the G2/M indicator of FASTFUCCI which reached undetectable levels in the cells. Thus, for the purpose of quantifying cell cycling only nuclei in the G1 phase, red, were quantified.

Notably, provision of an HA based matrix resulted in a higher proportion of cells in G1 phase, each well was normalized to their day 1 values, following our 15-day study than the GS condition (Figure 3A/B). Additionally, we validated the capacity for treatment with dasatinib to selectively abolish resistance to TMZ granted by hydrogel cultures as the TMZ and dasatinib

dual treatment condition saw a reduction in this metric. In contrast, Dasatinib alone did not induce significant cell death, although total proliferation was attenuated in comparison to the vehicle treated condition (data not shown). These results demonstrate that we were successful in our efforts to miniaturize our hydrogel technology to a high-throughput compatible format while retaining HA mediated drug resistance to TMZ. Furthermore, the increased throughput of our methods mean that scaling to testing multiple compounds in combination are now possible.

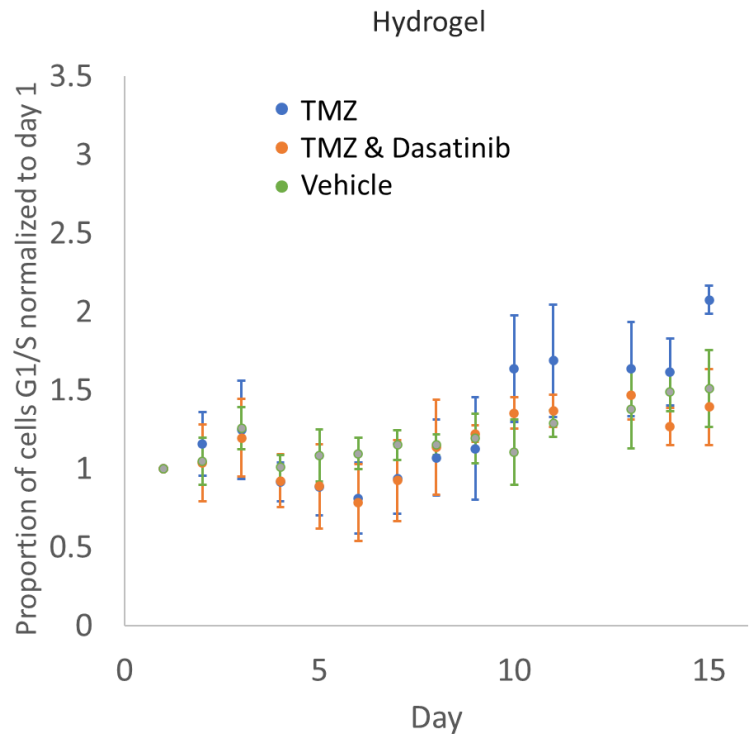
Hydrogel
TMZ
TMZ & Dasatinib
Vehicle
Proportion of cells G1/S normalized to day 1
3.5
3
2.5
2
1.5
1
0.5
0
0
5
10
15
Day

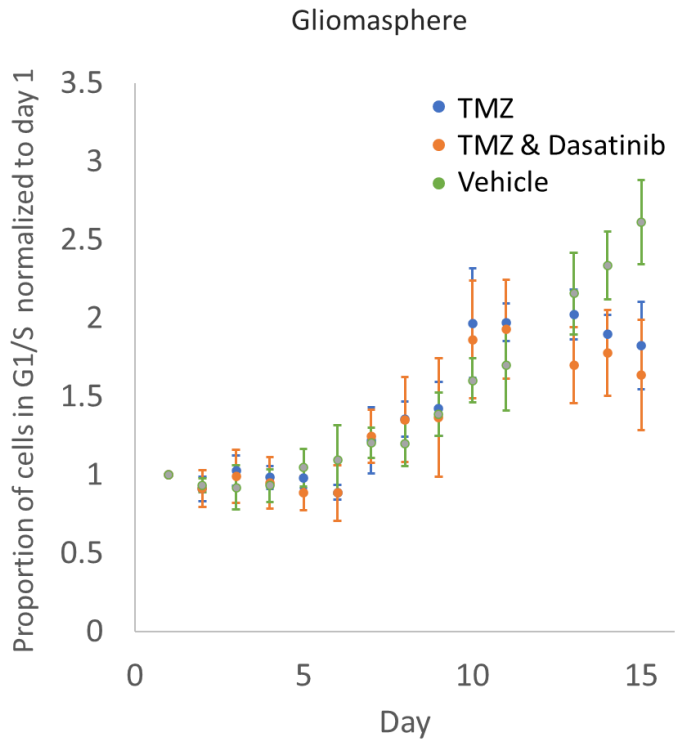
Gliomasphere
TMZ
TMZ & Dasatinib
Vehicle
Proportion of cells in G1/S normalized to day 1
3.5
3
2.5
2
1.5
1
0.5
0
0
5
10
15
Day

Figure 2-3: SRC inhibitor (Dasatinib) abolishes drug resistance acquisition.

Quantification of proportion of cells in G1/S phases increased over the assay period in gel augmented cultures when treated with TMZ compared to GS conditions. Addition of Dasatinib was found to abolish this effect in the gel conditions but had no discernable effects in the GS conditions.

Matrix Screen with U87 cells

Due to the fragility of the patient derived lines, we utilized the transformed GBM U87 cell line in a proof-of-concept matrix screen. As the U87 cell line has also been widely used in the literature we felt that this proof-of-concept study would be of the most utility to the greater GBM research community as access to patient derived cell lines is typically difficult for research labs outside large hospital institutions.[28] We first evaluated the ability of different peptides derived from proteins known to be upregulated in the GBM TME to affect proliferation of GBM U87. In contrast to patient derived cell lines, the U87 cell line exhibited a much faster doubling time. Thus, we evaluated the effect of peptide presentation on cell proliferation by comparing the number of cells quantified at day 4 relative to day 1 of our experiments when cultured in media. We tested all peptides individually as well as pairwise combinations versus the gliomasphere control. Given the number of conditions we assessed the performance of these various matricies by strictly standardized mean differences (SSMD) and Fold-Change metrics.[29] In high-throughput screens, however, variation can mask the actual effect.

We simultaneously plotted SSMD and fold change on the y and x axes respectively and identified that the highest performing conditions were Vitronectin and Osteopontin, Vitronectin and Tenascin C, and Tenascin C and OP combinations having SSMD values greater than 2 as well as fold changes greater than 1. These cut offs were chosen according to literature values.[29] According to these metrics most of our tested conditions fail to adequately distinguish themselves from the control group of gliomasphere. Surprisingly, although each of these conditions demonstrated a higher rate of proliferation compared to gliomasphere only the Tenascin C and Osteopontin condition demonstrated any survival benefit in the context of a

TMZ challenge as assessed by a CCK8 assay at then end of the 15 day experiment. Additionally, although the Tenascin C and Osteopontin condition demonstrated resistance to TMZ in the U87s all matrix cultures were found to have lower cell numbers at the end of the two week assay when treated with dasitinib as was found in the study with GS304.

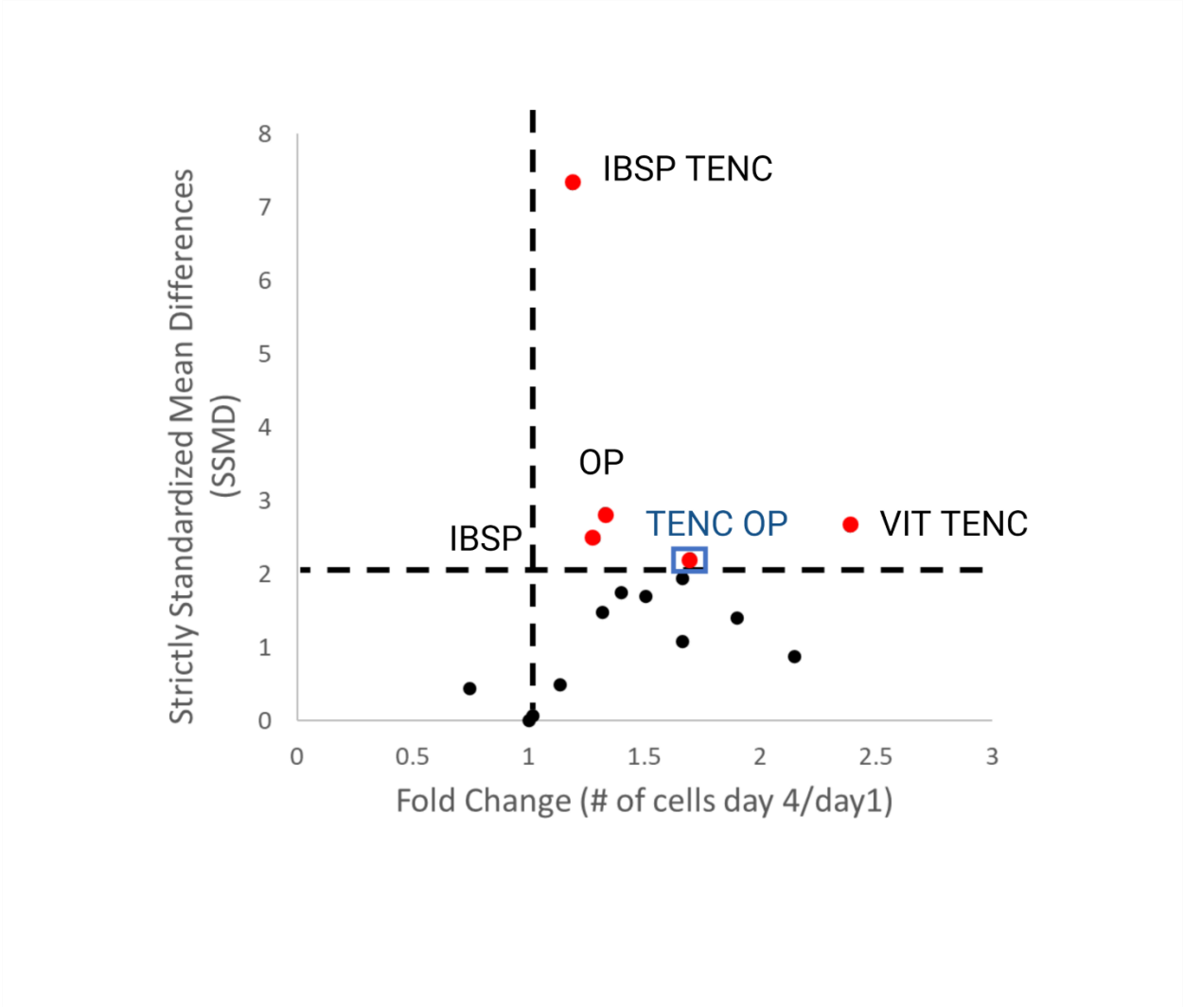

Figure 2-4: HT screening methods identify peptide/peptide pairs promoting proliferation and drug resistance in U87

Dual Flashlight plot SSMD vs Fold Change # of cells day4/day1 scaled by gliomasphere. TENC

OP (blue) is the only condition which remains significant in a drug challenge study.

2.4. Discussion

In this report we detail our efforts to adapt our HA based hydrogel technology to a format that is compatible with high throughput workflows such as drug screening. This was accomplished by adapting technologies such as automated liquid handlers to dispense viscous polymeric solutions while designing imaging workflows for daily sequential imaging as well as automated image analysis to handle the increase in acquired data points. In comparison to our previous methods, we demonstrated an increase in manufacturability on both times spent performing experiments (up to 6-fold increase in speed) as well as significant reductions in reagent usage (up to 160-fold). These reductions in cost and labor make it more commercially feasible for entities to utilize matrix augmented cultures in their drug screens. In addition, we also demonstrated the capacity to leverage this increase in throughput to perform matrix screening to identify a matrix composition for drug resistance studies.

In the context of other approaches utilized for drug screening of GBM our approach provides the capacity for single cell resolution as well as longitudinal readouts. [7,33–36] In its current form we did not leverage the full potential of these features of our data set, however the utility of these data points is part of a planned collaboration with data driven modeling experts. Furthermore, future experiments will expand upon the high content capabilities of the ImageXpress microscope to provide an even denser data set which can be used to identify novel phenotypes displayed by these cells. Indeed, towards this goal, we have also developed an additional assay method to investigate cytoskeletal dynamics using an actin binding peptide. [37]Given the propensity of GBM to diffusively migrate throughout the brain parenchyma utilization of this

screening array approach may help identify therapeutics which target these migratory behaviors.[38,39]

Limitations of this study include the fact that we were unable to utilize both patient derived cell lines due to cytotoxicity of the transduction behavior. Given these limitations, alternate methods of labeling the cells for automated image analysis will be required. Advancements in label free methods for cell segmentation may help in this regard.[40] Another limiting factor of the presented methods was the limited culture area of 2D surfaces as shown by the tendency for U87 cultures to overgrow the well plate. Methods to scale this work to three dimensions will require automated liquid handlers capable of dispensing larger volumes, while also developing imaging modalities that can handle the increase in sample thickness.

All in all, the presented work here demonstrates the methods and workflow for adaptation of traditionally artisanal hydrogel fabrication workflows to a high throughput compatible format. These advancements will help efforts to identify novel therapeutics for the treatment of GBM as well as the development of precision medicine therapies by identifying patient specific optimized matrix conditions for evaluation of drug resistance.

2.5. References

1. Ostrom, Q. T., Cioffi, G., Waite, K., Kruchko, C. & Barnholtz-Sloan, J. S. CBTRUS Statistical Report: Primary Brain and Other Central Nervous System Tumors Diagnosed in the United States in 2014–2018. *Neuro-Oncology* **23**, iii1–iii105 (2021).
2. Feng, E., Sui, C., Wang, T. & Sun, G. Temozolomide with or without Radiotherapy in Patients with Newly Diagnosed Glioblastoma Multiforme: A Meta-Analysis. *European Neurology* **77**, 201–210 (2017).

3. Chohan, M. O. & Berger, M. S. 5-Aminolevulinic acid fluorescence guided surgery for recurrent high-grade gliomas. *J Neurooncol* **141**, 517–522 (2019).

4. Su, J. *et al.* Molecularly Targeted Drugs Plus Radiotherapy and Temozolomide Treatment for Newly Diagnosed Glioblastoma: A Meta-Analysis and Systematic Review. *Oncology Research Featuring Preclinical and Clinical Cancer Therapeutics* **24**, 117–128 (2016).

5. Wu, W. *et al.* Glioblastoma multiforme (GBM): An overview of current therapies and mechanisms of resistance. *Pharmacological Research* **171**, 105780 (2021).

6. Mooney, J. *et al.* Current Approaches and Challenges in the Molecular Therapeutic Targeting of Glioblastoma. *World Neurosurgery* **129**, 90–100 (2019).

7. Badr, C. E., Wurdinger, T. & Tannous, B. A. Functional drug screening assay reveals potential glioma therapeutics. *Assay and Drug Development Technologies* **9**, 281–289 (2011).

8. Herbener, V. J. *et al.* Considering the Experimental use of Temozolomide in Glioblastoma Research. *Biomedicines* **8**, (2020).

9. Pibuel, M. A., Poodts, D., Díaz, M., Hajos, S. E. & Lompardía, S. L. The scrambled story between hyaluronan and glioblastoma. *The Journal of Biological Chemistry* **296**, 100549 (2021).

10. Juric, V. *et al.* Transcriptional CDK inhibitors, CYC065 and THZ1 promote Bim-dependent apoptosis in primary and recurrent GBM through cell cycle arrest and Mcl-1 downregulation. *Cell Death Dis* **12**, (2021).

11. Xiao, W., Sohrabi, A. & Seidlits, S. K. Integrating the glioblastoma microenvironment into engineered experimental models. *Future Sci OA* **3**, FSO189 (2017).

12. Yu, Q. *et al.* Extracellular Matrix Proteins Confer Cell Adhesion-Mediated Drug Resistance Through Integrin α v in Glioblastoma Cells. *Front Cell Dev Biol* **9**, (2021).

13. Xiao, W. *et al.* Brain-mimetic 3D culture platforms allow investigation of cooperative effects of extracellular matrix features on therapeutic resistance in glioblastoma. *Cancer Research* **78**, 1358–1370 (2018).

14. Xiao, W. *et al.* Bioengineered scaffolds for 3D culture demonstrate extracellular matrix-mediated mechanisms of chemotherapy resistance in glioblastoma. *Matrix Biology* **85–86**, 128–146 (2020).

15. Chen, Dr. J.-W. E., Leary, Mr. S., Barnhouse4, Mr. V., Sarkaria, Dr. J. N. & Harley, Dr. B. A. C. Matrix hyaluronic acid and hypoxia influence a CD133+ subset of patient-derived glioblastoma cells. *https://home.liebertpub.com/tea* (2021) doi:10.1089/TEN.TEA.2021.0117.

16. Pedron, S. *et al.* Hyaluronic acid-functionalized gelatin hydrogels reveal extracellular matrix signals temper the efficacy of erlotinib against patient-derived glioblastoma specimens. *Biomaterials* **219**, 119371 (2019).

17. Brancato, V., Oliveira, J. M., Correlo, V. M., Reis, R. L. & Kundu, S. C. Could 3D models of cancer enhance drug screening? *Biomaterials* **232**, 119744 (2020).

18. Warrick, J. W., Murphy, W. L. & Beebe, D. J. Screening the Cellular Microenvironment: A Role for Microfluidics. *IEEE Rev Biomed Eng* **1**, 75 (2008).

19. Hydrogel design of experiments methodology to optimize hydrogel for iPSC-NPC culture. *Advanced Healthcare Materials* **4**, 534–539 (2015).

20. Tannous, B. A. Gaussia luciferase reporter assay for monitoring biological processes in culture and in vivo. *Nature Protocols* **4**, 582–591 (2009).

21. Patel, A. P. *et al.* Single-cell RNA-seq highlights intratumoral heterogeneity in primary glioblastoma. *Science* **344**, 1396 (2014).

22. Cosset, É., Weis, S. M. & Cheresh, D. A. Re-thinking the preclinical development of GBM therapeutics. *Oncoscience* **5**, 11–12 (2018).

23. Cosset, É., Weis, S. M. & Cheresh, D. A. Re-thinking the preclinical development of GBM therapeutics. *Oncoscience* **5**, 11–12 (2018).

24. Xiao, W. *et al.* Brain-mimetic 3D culture platforms allow investigation of cooperative effects of extracellular matrix features on therapeutic resistance in glioblastoma. *Cancer Research* **78**, 1358–1370 (2018).

25. Xiao, W. *et al.* Bioengineered scaffolds for 3D culture demonstrate extracellular matrix-mediated mechanisms of chemotherapy resistance in glioblastoma. *Matrix Biology* **85–86**, 128–146 (2020).

26. Carpenter, A. E. *et al.* CellProfiler : image analysis software for identifying and quantifying cell phenotypes. **7**, (2006).

27. Xiao, W., Ehsanipour, A., Sohrabi, A. & Seidlits, S. K. Hyaluronic-Acid Based Hydrogels for 3-Dimensional Culture of Patient-Derived Glioblastoma Cells. *JoVE (Journal of Visualized Experiments)* **2018**, e58176 (2018).

28. Ghochani, Y. *et al.* Generation of a molecular interactome of the glioblastoma perivascular niche reveals Integrin Binding Sialoprotein as a key mediator of tumor cell migration. *bioRxiv* 2021.10.01.462643 (2021) doi:10.1101/2021.10.01.462643.

29. Zhang, X. D. Illustration of SSMD, z score, SSMD*, z* score, and t statistic for hit selection in RNAi high-throughput screens. *Journal of Biomolecular Screening* **16**, 775–785 (2011).

30. Characterization of the crosslinking kinetics of multi-arm poly(ethylene glycol) hydrogels formed via Michael-type addition. *Soft Matter* (2016) doi:10.1039/C5SM02668G.

31. Zhang, J., F.G. Stevens, M. & D. Bradshaw, T. Temozolomide: Mechanisms of Action, Repair and Resistance. *Current Molecular Pharmacology* **5**, 102–114 (2012).

32. Koh, S. B. *et al.* A quantitative FastFUCCI assay defines cell cycle dynamics at a single-cell level. *Journal of Cell Science* (2017) doi:10.1242/jcs.195164.

33. Akay, M. *et al.* Drug Screening of Human GBM Spheroids in Brain Cancer Chip. *Scientific Reports* **8**, 15423 (2018).

34. Li, Y. & Kumacheva, E. Hydrogel microenvironments for cancer spheroid growth and drug screening. *Science Advances* **4**, (2018).

35. Schwartz, A. D. *et al.* A biomaterial screening approach reveals microenvironmental mechanisms of drug resistance. *Integr Biol (Camb)* **9**, 912–924 (2017).

36. Calpe, B. & Kovacs, W. J. High-throughput screening in multicellular spheroids for target discovery in the tumor microenvironment. *https://doi.org/10.1080/17460441.2020.1756769* **15**, 955–967 (2020).

37. Riedl, J. *et al.* Lifeact: A versatile marker to visualize F-actin. *Nature Methods* (2008) doi:10.1038/nmeth.1220.

38. Reardon, D. A. *et al.* Cilengitide: An RGD pentapeptide αvβ3 and αvβ5 integrin inhibitor in development for glioblastoma and other malignancies. *Future Oncology* **7**, 339–354 (2011).

39. Reardon, D. A., Nabors, L. B., Stupp, R. & Mikkelsen, T. Cilengitide: An integrin-targeting arginine-glycine-aspartic acid peptide with promising activity for glioblastoma multiforme. *Expert Opinion on Investigational Drugs* **17**, 1225–1235 (2008).

40. Powell, R. T. *et al.* deepOrganoid: A brightfield cell viability model for screening matrix-embedded organoids. *SLAS Discov* **27**, 175–184 (2022).

Chapter 3. Hydrogel Arrays Enable Increased Throughput for Screening Effects of Matrix Components and Therapeutics in 3D Tumor Models

3.1. AUTHORS AND AFFILIATIONS:

Jesse Liang[1], Alireza Sohrabi[1], Mary Epperson[1], Laila M. Rad[1], Kelly Tamura[1], Mayilone Sathialingam[1], Thamira Skandakumar[1], Philip Lue[1], Jeremy Huang[1], James Popoli[1], Aidan Yackly[1], Michael Bick[1], Ze Zhong Wang[1], Chia-Chun Chen[1], Grigor Varuzhanyan[1], Robert Damoiseaux[1], Stephanie K. Seidlits[1]*

[1]University of California Los Angeles, CA, United States

3.2. SUMMARY:

The present protocol describes an experimental platform to assess the effects of mechanical and biochemical cues on chemotherapeutic responses of patient-derived glioblastoma cells in 3D matrix-mimetic cultures using a custom-made UV illumination device facilitating high-throughput photocrosslinking of hydrogels with tunable mechanical features.

3.3. ABSTRACT:

Cell-matrix interactions mediate complex physiological processes through biochemical, mechanical, and geometrical cues, influencing pathological changes and therapeutic responses. Accounting for matrix effects earlier in the drug development pipeline is expected to increase the likelihood of clinical success of novel therapeutics. Biomaterial-based strategies recapitulating specific tissue microenvironments in 3D cell culture exist but integrating these with the 2D culture methods primarily used for drug screening has been challenging. Thus, the protocol

presented here details the development of methods for 3D culture within miniaturized biomaterial matrices in a multi-well plate format to facilitate integration with existing drug screening pipelines and conventional assays for cell viability. Since the matrix features critical for preserving clinically relevant phenotypes in cultured cells are expected to be highly tissue- and disease-specific, combinatorial screening of matrix parameters will be necessary to identify appropriate conditions for specific applications. The methods described here use a miniaturized culture format to assess cancer cell responses to orthogonal variation of matrix mechanics and ligand presentation. Specifically, this study demonstrates the use of this platform to investigate the effects of matrix parameters on the responses of patient-derived glioblastoma (GBM) cells to chemotherapy.

3.4. INTRODUCTION:

The expected cost of developing a new drug has steadily risen over the past decade, with over $1 billion in current estimates[1]. Part of this expense is the high failure rate of drugs entering clinical trials. Approximately 12% of drug candidates ultimately earn approval from the United States (US) Food & Drug Administration (FDA) in 2019. Many drugs fail in Phase I due to unanticipated toxicity[2], while others that pass safety trials may fail due to a lack of efficacy[3]. This attrition due to non-efficacy can partly be explained by the fact that cancer models used during drug development are notoriously non-predictive of clinical efficacy[4].

Functional disparities between *in vitro* and *in vivo* models may be attributed to removing cancer cells from their native microenvironment, including non-tumor cells and the physical ECM[5,6]. Commonly, research groups use commercially available culture matrices, such as Matrigel (a proteinaceous basement membrane matrix) derived from mouse sarcomas to provide cultured

tumor cells with a 3D matrix microenvironment. Compared to 2D culture, 3D culture in membrane matrix has improved the clinical relevance of *in vitro* results[7,8]. However, culture biomaterials from decellularized tissues, including the membrane matrix, typically exhibit batch-to-batch variability that may compromise reproducibility[9]. Furthermore, matrices derived from tumors with different tissue origins from those studied may not provide the appropriate physiological cues[10]. Finally, cancers with high degrees of intratumoral heterogeneity have microenvironmental features that vary on a submicron-size scale and which the membrane matrix cannot be tuned to recapitulate[11].

Glioblastoma (GBM), a uniformly lethal brain tumor with a median survival time of approximately 15 months, is a cancer for which treatment development has been particularly difficult[12,13]. The current standard of care for GBM consists of primary tumor resection, followed by radiotherapy, and then chemotherapy using temozolomide (TMZ)[14]. Yet, more than half of clinical GBM tumors exhibit treatment resistance through various mechanisms[15–17]. Predicting the efficacy of a treatment regimen for an individual patient is extremely difficult. Standard preclinical models used to predict individual outcomes consist of patient-derived tumor cells xenografted orthotopically into immunocompromised mice. While patient-derived xenografts can recapitulate many aspects of clinical GBM tumors and are valuable for preclinical models[18], they are inherently expensive, low throughput, time-consuming, and involve ethical concerns[19]. Cultures of patient-derived cells, on 2D plastic surfaces or as spheroids, mostly avoid these issues. However, despite preserving patient-specific genetic aberrations in these cultures, clinical translation of *in vitro* results has been poor representations of both *in vivo* models and original patient tumors[20]. Previously, we, and others, have shown that GBM cells cultured in a 3D ECM

that mimics the mechanical and biochemical properties of brain tissue can preserve drug resistance phenotypes[10,21–23].

Interactions between hyaluronic acid (HA), a polysaccharide abundant in the brain ECM and overexpressed in GBM tumors, and its CD44 receptor modulate the acquisition of drug resistance *in vitro*[21,24–27]. For example, the inclusion of HA within soft, 3D cultures increased the ability of patient-derived GBM cells to acquire therapeutic resistance. This mechano-responsivity was dependent on HA binding to CD44 receptors on GBM cells[21]. Additionally, integrin binding to RGD-bearing peptides, incorporated into 3D culture matrices, amplified CD44-mediated chemoresistance in a stiffness-dependent manner[21]. Beyond HA, the expression of several ECM proteins, many containing RGD regions, vary between normal brain and GBM tumors[28]. For example, one study reported that 28 distinct ECM proteins were upregulated in GBM tumors[29]. Within this complex tumor matrix microenvironment, cancer cells integrate mechanical and biochemical cues to yield a particular resistance phenotype, which depends on relatively small differences (e.g., less than an order of magnitude) in Young's modulus or density of integrin-binding peptides[28–30].

The present protocol characterizes how tumor cells interpret unique combinations of matrix cues and identify complex, patient-specific matrix microenvironments that promote treatment resistance (**Figure 1A**). A photochemical method for generating miniaturized, precisely tuned matrices for 3D culture provides a large, orthogonal variable space. A custom-built array of LEDs, run by a microcontroller, was incorporated to photocrosslink hydrogels within a 384-well plate format to increase automation and reproducibility. Exposure intensity was varied across well to alter micro-mechanical properties of resulting hydrogels, as assessed using atomic force

microscopy (AFM). While this manuscript does not focus on constructing the illumination array itself, a circuit diagram (**Figure 1B**) and parts list (**Table of Materials**) are provided as aids for device reproduction.

This report demonstrates the rapid generation of an array of GBM cells cultured in unique, 3D microenvironments in which Young's modulus (four levels across a single order of magnitude) and integrin-binding peptide content (derived from four different ECM proteins) were varied orthogonally. The approach was then used to investigate the relative contributions of hydrogel mechanics and ECM-specific integrin engagement on the viability and proliferation of patient-derived GBM cells as they acquire resistance to temozolomide (TMZ) chemotherapy.

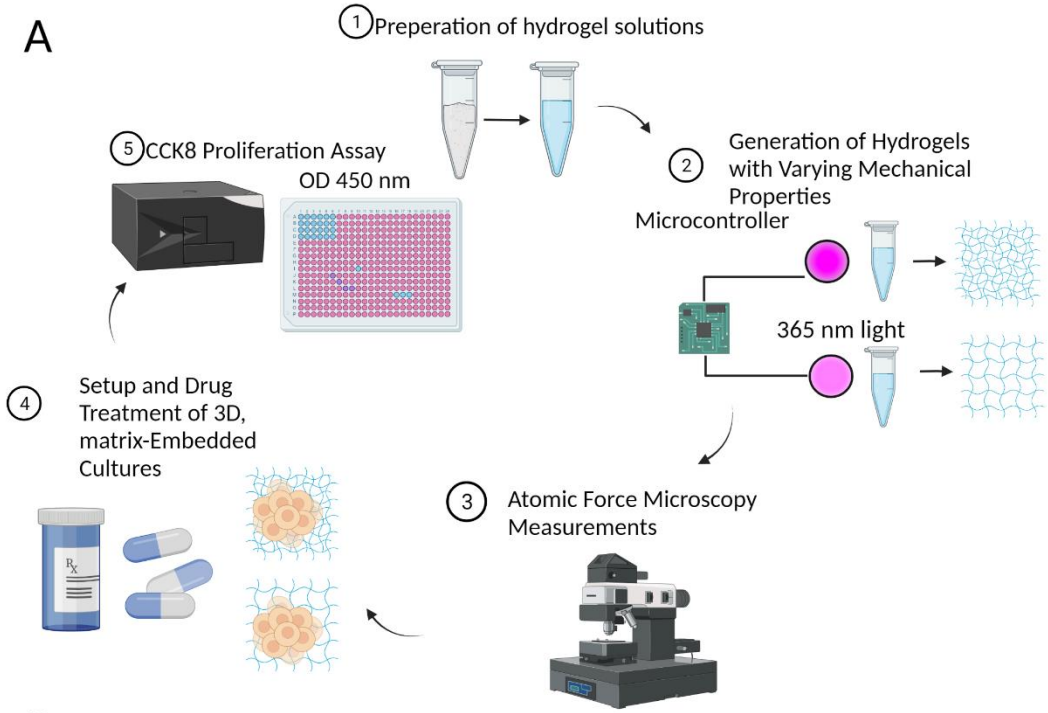
A
1 Preperation of hydrogel solutions
2 Generation of Hydrogels with Varying Mechanical Properties
Microcontroller
365 nm light
3 Atomic Force Microscopy Measurements
4 Setup and Drug Treatment of 3D, matrix-Embedded Cultures
5 CCK8 Proliferation Assay
OD 450 nm

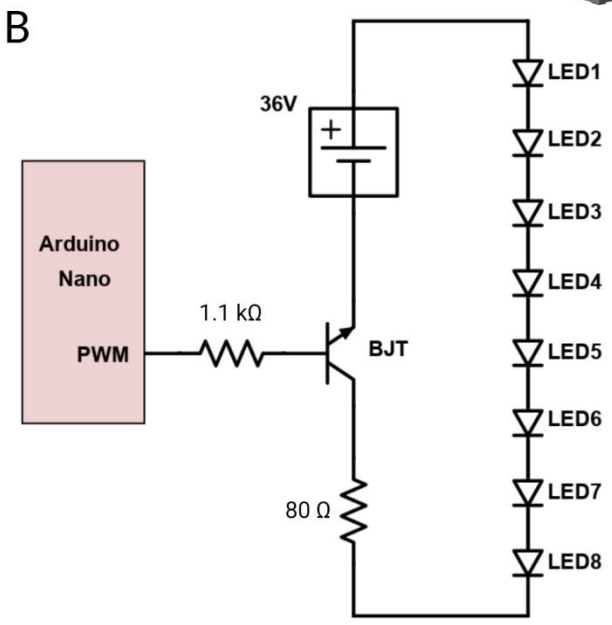
B
36V
Arduino Nano
PWM
1.1 kΩ
BJT
80 Ω
LED1
LED2
LED3
LED4
LED5
LED6
LED7
LED8

Figure 3-1: Cartoon depiction of the protocol.
(A) Cartoon depiction of the process for 3D culture generation and monitoring. (1) HA-based hydrogel solutions are prepared. (2) Hydrogel solutions are then crosslinked with variable intensity through LEDs controlled by an Arduino microcontroller. (3) Resulting hydrogel mechanics are assessed by AFM to verify the difference in gel mechanics. (4) Solutions matching the formulation from Step 1 are then used to encapsulate patient-derived GBM cells and treated with the drug. (5) Following 7 days, cell viability is read out via CCK8 colorimetric assay. (B) Circuit diagram for custom LED illumination array used in this protocol. The individual components are listed in the Table of Materials.

3.5. PROTOCOL:

Patient-derived GBM cell lines (GS122 and GS304) were provided by Professor David Nathanson (our collaborator), who developed these lines under a protocol approved by the UCLA Institutional Review Board (IRB# 10-000655). Cells were provided de-identified so that the cell lines could not be linked back to the individual patients.

1. Preparation of hydrogel solution

1.1. Prepare HEPES-buffered solution by dissolving HEPES powder at 20 mM in Hank's balanced salt solution (HBSS). Adjust pH to 7 following full solvation.

1.2. In the HEPES-buffered solution, dissolve thiolated HA (700 kDa nominal molecular weight, see **Table of Materials**), prepared following the previous report[31], so that 6%–8% of carboxylic acid residues on each glucuronic acid are modified with a thiol, at a concentration of 10 mg/mL in buffer solution.

NOTE: An amber vial is recommended to prevent thiol oxidation by ambient light.

1.2.1. Stir using a magnetic stir plate (<1,000 rpm) at room temperature until fully dissolved, typically around 45 min.

1.3. While HA is dissolving, prepare separate solutions of (1) 100 mg/mL of 8-arm-PEG-Norbornene (20 kDa), (2) 100 mg/mL of 4-arm-PEG-Thiol (20 kDa), (3) 4 mM of cysteine or cysteine-containing peptide (e.g., GCGYGRGDSPG), and (4) 4 mg/mL of LAP in microcentrifuge tubes (see **Table of Materials**).

1.3.1. Prepare each of these four solutions in the HEPES-buffered solution prepared in step 1.1. Vortex the solutions to ensure full dissolution of each reagent prior to performing step 4.

NOTE: If testing multiple different peptides, each must contain a cysteine or other source of thiol moiety for this conjugation chemistry.

1.3.2. Prepare solutions (4 mM available thiol) of all peptides to be tethered within a single hydrogel at this point.

NOTE: Peptide sequences and ECM proteins from which they were derived and used in this study are listed in **Table 1**. N-acetyl cysteine (see **Table of Materials**), to which cells do not bind, can be substituted for a bioactive, thiol-containing peptide to titrate the concentration of an adhesive peptide or act as a negative control[31].

1.4. Mix the individual solutions of HA, PEG-Norbornene, PEG-thiol, and cysteine/thiol-containing peptides (see **Table of Materials**) to achieve the final concentrations for the final hydrogel matrices listed in **Table 2**. Stir (<1,000 rpm) on a magnetic stir plate for at least 30 min to mix fully.

NOTE: HA solutions are highly viscous and best handled using a positive displacement pipette (see **Table of Materials**). If a positive displacement pipette is unavailable, viscous solutions can also be dispensed with a standard micropipette by slowly pipetting using wide-orifice tips.

2. Illumination and photocrosslinking of hydrogels *via* an LED array

CAUTION: Wear UV protective eyewear and cover the illumination field with UV-absorbing material.

NOTE: The LED array described in this protocol consists of six sets of eight LEDs placed in series, as illustrated by the provided circuit diagram (**Figure 1A**). Each set of LEDs can be independently powered, which allows for up to six different irradiances per run. **Supplementary File 1** contains screenshots corresponding to the following directions for further guidance.

2.1. Download the Illumination Device.zip file from the **Supplementary Coding Files**. This directory contains the following files: Arduino.zip (**Supplementary Coding File 1**), Drivers.zip (**Supplementary Coding File 2**), GUI.zip (**Supplementary Coding File 3**), and Holder.zip (**Supplementary Coding File 4)**.

NOTE: 3D Print the top and bottom portions for holding the circuit board in place (see **Supplementary Coding Files** for details).

2.2. Download and install the microcontroller software (see **Table of Materials**).

2.3. Download and install the GUI software (see **Table of Materials**). Refer to **Supplementary File 1** for software operating instructions.

2.4. Open **Processing** and install the controlIP5 library *via* clicking on **Sketch** > **Import Library** > **Add Library**. Then, search for controlIP5 in libraries and click on **Install**. Perform this for the very first time.

2.5. Power the illumination device (see **Table of Materials**) using the 36 Volt power supply and connect it to a PC using a micro-USB cable.

NOTE: Some devices will not install drivers automatically for various Arduino nano boards. One set of drivers is provided in the device zip file.

2.6. Open the Arduino.ino file, located in the Adruino.zip folder, using Arduino IDE.

2.7. Compile the Arduino.ino file by clicking on the **Checkmark** button. Upload the compiled code by clicking on the **Arrow** button.

2.8. Open the GUI.pde file, located in the GUI.zip folder, using Processing.

2.9. Click on **Run** in the processing program to launch the graphical user interface for controlling the illumination device.

2.10. In the graphical user interface window, click on **Intensity** for the column containing hydrogel precursor solution to be crosslinked and input the desired intensity. Click on the **Time** box and input desired time. For the solution provided in **Table 2**, this will be 15 s.

NOTE: End-users need to calibrate digital intensity values to irradiance using a radiometer. Examples of typical intensities are provided in **Figure 2A**.

2.11. Align the samples with the illumination device (**Figure 2B**) with every other LED in a single column of the silicone molds (see **Table of Materials**) or 384-well plate. Click on **Finish** to begin illumination. Repeat this process as necessary for illumination of multiple slides or other wells of a 384-well plate.

NOTE: The holder is designed such that the 384-well plate sits flush with one corner of the inner chamber during illumination.

2.11.1. Following illumination, when placed in one corner, move the well plate to the next corner and repeat. To illuminate wells on the other half of the plate, lift the plate out of the holder and rotate 180°.

2.12. Generate hydrogels with varying mechanics for mechanical characterization following the steps below.

2.12.1. Clean the glass slides and silicone molds using tape to remove debris. Adhere the silicone molds to the glass slide, press down to ensure a good seal, and displace any air bubbles.

2.12.2. Pipette 80 µL of hydrogel precursor solution, as prepared in step 1.4, into each silicone mold on the glass slide.

2.12.3. Place the glass slide onto the illumination device aligned with every other LED in a single column. Expose the hydrogel precursors to UV light for 15 s, as described in step 2, to photocrosslink.

2.12.4. Once illumination has stopped, retrieve the slides, and loosen the gels from the molds by tracing the inner circumference of the mold with a fine tip (10 µL pipette tip, 30 G needle, etc.). Remove silicone molds with tweezers/forceps.

2.12.5. Move crosslinked hydrogels into individual wells of a 12-well plate by wetting a spatula and gently pushing them off the glass slide. Fill each well with 2 mL of DPBS (see **Table of Materials**) prior to adding the hydrogel. Swell the gels in DPBS solution for at least 12 h (typically overnight) at room temperature (for the next day's mechanical characterization).

3. Atomic Force Microscopy (AFM) measurements

3.1. Turn on the atomic force microscope (AFM) according to the manufacturer's instructions (see **Table of Materials**). This protocol provides brief instructions for using the instrument and the related software.

3.2. Install the AFM probe (see **Table of Materials**).

NOTE: For the present study, a triangular silicon nitride cantilever with a nominal spring constant of 0.01 N/m was modified with a spherical 2.5 µm silicon dioxide particle.

3.3. Following installation, align the laser to the apex of the triangular probe, and then adjust mirror and laser deflection to maximize signal sum (typically between 1.5–2.2 Volts).

3.4. Immerse the probe in DPBS and wait for up to 15 min to obtain thermal equilibrium. Click on the **Calibration** button and select **Contact-Dependent** calibration. Click on the **Collect Thermal Tuning** button, and following data collection, select the peak around 3 kHz for calibration.

NOTE: Slight adjustment of the mirror and laser deflectors may be necessary following immersion into a liquid due to refractive index changes.

3.5. Approach the surface of a Petri dish (plastic) by setting the **Approach Parameters** to **Constant Velocity**, a target height of **7.5 µm**, and an approach speed of **15 µm/s**. Enable **Baseline Measurement Per Run for Approach** so that the approach runs continuously and does not stop early due to drift in the deflector.

3.6. Upon approach, set acquisition parameters for force mapping to 4 nN turnarounds, 2 µm indentation distance, 1 µm/s velocity, and 0 s contact time. Press the **Start** button to begin collecting a force curve on the plastic surface (e.g., a well plate).

3.7. Return to the calibration window and select the portion of the force curve corresponding to contact and indentation of the plastic. Accept the calculated sensitivity and stiffness values for the probe to complete calibration.

3.8. Following calibration, raise the AFM probe and place the hydrogel sample for interrogation. Approach hydrogel following the settings provided in step 5.

NOTE: During the approach procedure toward the hydrogel surface, the unit may mistakenly trigger the approached state. To verify the actual approach, obtain a force curve as in step 4.6. Repeat the approach procedure if the resulting curve does not show contact and resulting indentation.

3.9. When the surface approach is successful, switch to the **Force Mapping** mode and set acquisition parameters to a map of 8 x 8 size with 40 µm length per axis. Obtain force maps in various regions to assess the uniformity of stiffness measurements.

3.9.1. Interpret force curves using the software program **JPK SPM Data Processing** through a Hertz/Sneddon model fit (Equations 1 and 2, see **Table 3** for the definition of all the variables) with the spherical geometry selected[32–34].

$$F = E\frac{E}{1-\nu^2}\left[\frac{a^2+{R_S}^2}{2}\ln\frac{R_S+a}{R_S-a} - aR_S\right] \quad \text{Equation 1}[32]$$

$$\delta = \frac{a}{2}\ln\frac{R_S+a}{R_S-a} \quad \text{Equation 2}[32]$$

4. Setting up and drug treatment of 3D, matrix-embedded cultures

4.1. Prepare desired cells as a single cell solution.

NOTE: Different cell types may require different passaging methods. A typical protocol for passaging a suspension culture of GBM spheroids from a T-75 flask is reported in reference[31].

4.2. Collect GBM spheroids (roughly 150 µm in diameter) from a T-75 flask suspension culture into a 15 mL conical tube. Rinse the culture flask with 5 mL of DPBS to remove any residual cells and media and add this volume to the conical tube.

4.3. Centrifuge the conical tube containing cells at 200 x *g* for 5 min at room temperature. Following centrifugation, remove the supernatant with a 5 mL serological pipette, taking care not to disturb the cell pellet, and resuspend in 5 mL of DPBS.

4.4. Centrifuge at 200 x *g* for 5 min at room temperature to wash cells. Aspirate the supernatant with a 5 mL serological pipette, taking care not to disturb the cell pellet, and then resuspend cells in 2 mL of cell dissociation reagent (see **Table of Materials**).

4.5. Incubate at room temperature for 10–15 min. Add 3 mL of complete medium (see **Table of Materials**) and gently pipette 3–5 times to break down the spheroids to a single cell suspension[31].

4.6. Centrifuge the single-cell suspension at 400 x *g* (single-cell suspensions may be spun faster for pellet formation) for 5 min to pellet cells at room temperature. Aspirate the supernatant with a 5 mL serological pipette, taking care not to disturb the cell pellet. Resuspend cells in 1 mL of complete medium.

NOTE: If the cells remain in clumps, rather than as single cells in suspension, following passaging, cells can be passed through a 40 µm cell strainer to achieve a single cell suspension.

4.7. Remove a portion of the cells for counting using a hemocytometer. Dilute this portion two-fold with trypan blue, which permeates cells with compromised viability. Count only the live, colorless cells. Typically, a T-75 seeded at 800,000 cells per flask yields 2–3 million cells after a week in culture.

4.8. Determine the number of cells necessary for encapsulation. Transfer a volume of media containing the total number of cells needed into a sterile 1.7 mL microcentrifuge tube. Spin down at 400 x *g* for 5 min at room temperature.

NOTE: For example, a minimum of 2.5 million cells resuspended in 1 mL of gel volume is needed to encapsulate cells at 2.5 million cells/mL. A gel volume of 1 mL allows users to dispense 100 gel drops, where each gel drop is of 10 µL volume. Preparing an extra ~20% volume of cells suspended in hydrogel solution is recommended to account for loss during pipette transfer. Thus, one would prepare 3 million cells and 1.2 mL of hydrogel precursor solution in this example. A minimum density of 500 thousand cells/mL is recommended.

4.9. Aspirate the supernatant with a micropipette, taking care not to disturb the cell pellet. Resuspend the cell pellet in the hydrogel precursor solution, as prepared in step 1.4, mixing well by pipetting up and down with a 1,000 µL micropipette 4–5 times.

4.10. Load the cells into a repeat pipettor (see **Table of Materials**) set to dispense 10 µL. To avoid bubbles and uneven dispensing, prime the repeat pipettor by dispensing an additional 1–2 times into a waste container.

4.11. In each well of a 384-well plate, dispense 10 µL of cells suspended in hydrogel solution from the repeat pipettor. Using the LED array, illuminate each well containing cells (step 2) for 15 s with intensities (example results in **Figure 2A** utilized intensities of 1.14, 1.55, 2.15, 2.74 mW/cm^2) to achieve the desired mechanical properties.

NOTE: It is suggested to start with five replicates per experimental condition and scale up or down depending on the desired throughput and variance of the endpoint assay.

4.12. Add 40 µL of complete media to each well containing the cells. Add 50 µL of DPBS to non-experimental, dry wells surrounding the gels to minimize losses due to evaporation.

4.13. For GBM cells, add 40 µL of the media-containing drug (e.g., TMZ, see **Table of Materials**) to achieve the final desired concentration (10 µM–100 µM in dimethylsulfoxide (DMSO) or vehicle (DMSO), accordingly, starting 3 days after encapsulation.

5. CCK8 proliferation assay

5.1. Add 10 µL of CCK8 reagent (see **Table of Materials**) to each well containing the cells.

NOTE: If performing this assay for the first time, include negative control wells such as media only or cell-free hydrogel in media.

5.2. Incubate for 1–4 h according to the manufacturer's instructions.

NOTE: This time may vary as a function of cell type and density, and thus incubation times need to be tested for each application so that absorbance values fall within a linear range, a requirement for applying Beer's Law[35].

5.3. Read absorbances at 450 nm for all wells following incubation.

5.4. Calculate the average absorbance at 450 nm obtained in step 3 for the vehicle condition for each group. Divide each drug-treated well by the average of the vehicle control per group.

5.5. Calculate confidence intervals by generating bootstrap distributions (N = 10,000) through the percentile method[36].

NOTE: Generally, one may utilize 95% confidence intervals and interpret conditions whose confidence intervals do not cross over 1 to be significant and warrant further investigation. Setting confidence intervals to 95% is congruent with setting a significance cutoff of $p = 0.05$. For the data shown in the results, there is utility in distinguishing conditions that either promote or inhibit matrix-mediated drug resistance, requiring a two-side analysis.

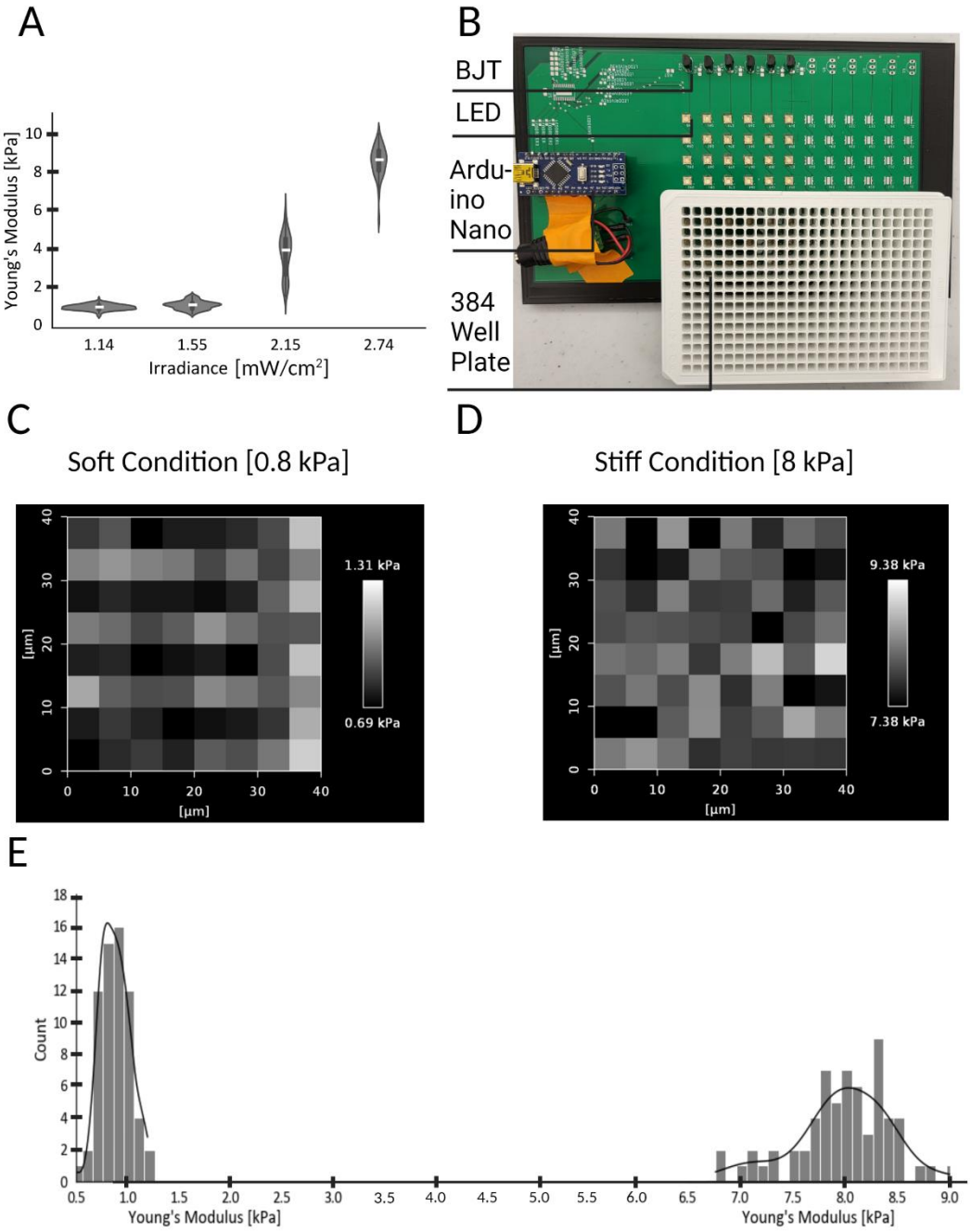
A
Young's Modulus [kPa]
0
2
4
6
8
10
1.14
1.55
2.15
2.74
Irradiance [mW/cm²]
B
BJT
LED
Ardu-
ino
Nano
384
Well
Plate
C
Soft Condition [0.8 kPa]
1.31 kPa
0.69 kPa
[µm]
D
Stiff Condition [8 kPa]
9.38 kPa
7.38 kPa
[µm]
E
Count
Young's Modulus [kPa]
Young's Modulus [kPa]

Figure 3-2: Hydrogels fabricated with varying stiffness using tunable LEDs to modify irradiance. (A) Violin plots show the calculated Young's Modulus from force curves generated by AFM across three surface regions, spanning 40 µm x 40 µm, of individual hydrogels. Young's modulus of each hydrogel is shown as a function of UV irradiance during photocrosslinking. Horizontal white lines indicate the median for each experimental group. (B) LED array with spacing matching the pitch of multi-well plates (384-wells). (C) Heat map showing the regional variation of Young's modulus (mean = 0.8 kPa) for a typical gel crosslinked by exposure to 1.55 mW/cm2 for 15 s. (D) Heat map showing regional variation of Young's modulus (mean = 8 kPa) for a typical gel crosslinked upon exposure to 2.74 mW/cm2 for 15 s. (E) Histogram illustrating the range of Young's modulus measurements across the surface of hydrogels shown in C and D.

3.6. REPRESENTATIVE RESULTS:

AFM measurements confirmed precise control of hydrogel mechanics as a function of UV irradiance (mW/cm^2) during photo-crosslinking using a custom-built, Arduino-controlled LED array (**Figure 2A**). The hydrogel formulation used in this protocol can be found in **Table 2**. The spacing of the LEDs on the provided template matches the spacing for every other well of a 384-well plate, allowing for the formation of gels inside the plate (**Figure 2B**). AFM interrogation of micron-scale regions at the surfaces of single hydrogels showed that hydrogels with softer average Young's moduli also had smaller ranges of moduli than stiffer hydrogels (**Figure 2C–E**). Cell seeding densities that maximize viability should be determined empirically for each cell type. This study demonstrates that 3D cultures of GS122 cells seeded at densities of 2,500,000 cells/mL exhibited substantially higher viabilities when assessed after 7 days in culture compared to those seeded at densities of 500,000 cells/mL (**Figure 3A**). Furthermore, GS122 and GS304 cells were used as models for culturing patient-derived GBM cells to investigate the dependence of chemotherapy response on the stiffness and biochemical composition of the matrix microenvironment (**Figure 3B–D**). Cell viability was assessed through the CCK8 assay after treatment with TMZ for 4 days leading to a total culture time of 7 days by scaling OD_{450} measurement by a corresponding vehicle control and generating 95% confidence intervals by bootstrapping (N = 10,000) with the percentile method[36]. With these distributions, conditions in which confidence intervals did not overlap with a value of 1 (dashed line) were considered significant. Compared to more commonly used statistical methods such as *t*-tests or ANOVA, estimation of confidence intervals, using bootstrapping to estimate distributions that would be

present for larger sample sizes, is preferred for screening assays whose goal is to identify a smaller subset of conditions for further investigation. One additional benefit of this method is that conditions with a smaller spread in a confidence interval can be prioritized over other conditions with a similar mean value but a higher spread in the confidence interval. This study indicated that GS122 cells gained survival benefits from microenvironmental interactions (**Figure 3B**). This survival benefit was significant in the 0.8, 1, and 4 kPa conditions but not in the 8 kPa condition for GS122 cells. GS304 cells were insensitive to both stiffness and TMZ treatment.

The effect of the biochemical composition of the matrix microenvironment was then examined by varying the inclusion of ECM-derived, integrin-binding peptides (**Table 1**) known to be upregulated in the GBM tumor microenvironment at two stiffnesses, 0.8 kPa, and 8 kPa. Again, GS304 cells received no significant survival benefit from matrix inclusion and were insensitive to TMZ. However, GS122 cells showed survival gains in the 8 kPa condition when osteopontin-derived peptides were included in the matrix, while the incorporation of integrin-binding sialoprotein (IBSP)- or tenascin-C-derived peptides provided minimal survival benefits, such as culture in matrices with the general RGD peptide (**Figure 3C**). In contrast, no peptides conferred survival gains in the 0.8 kPa culture condition (**Figure 3D**). Together, the results suggest intrinsic differences in both matrix and drug responses between the two patient-derived cell lines evaluated.

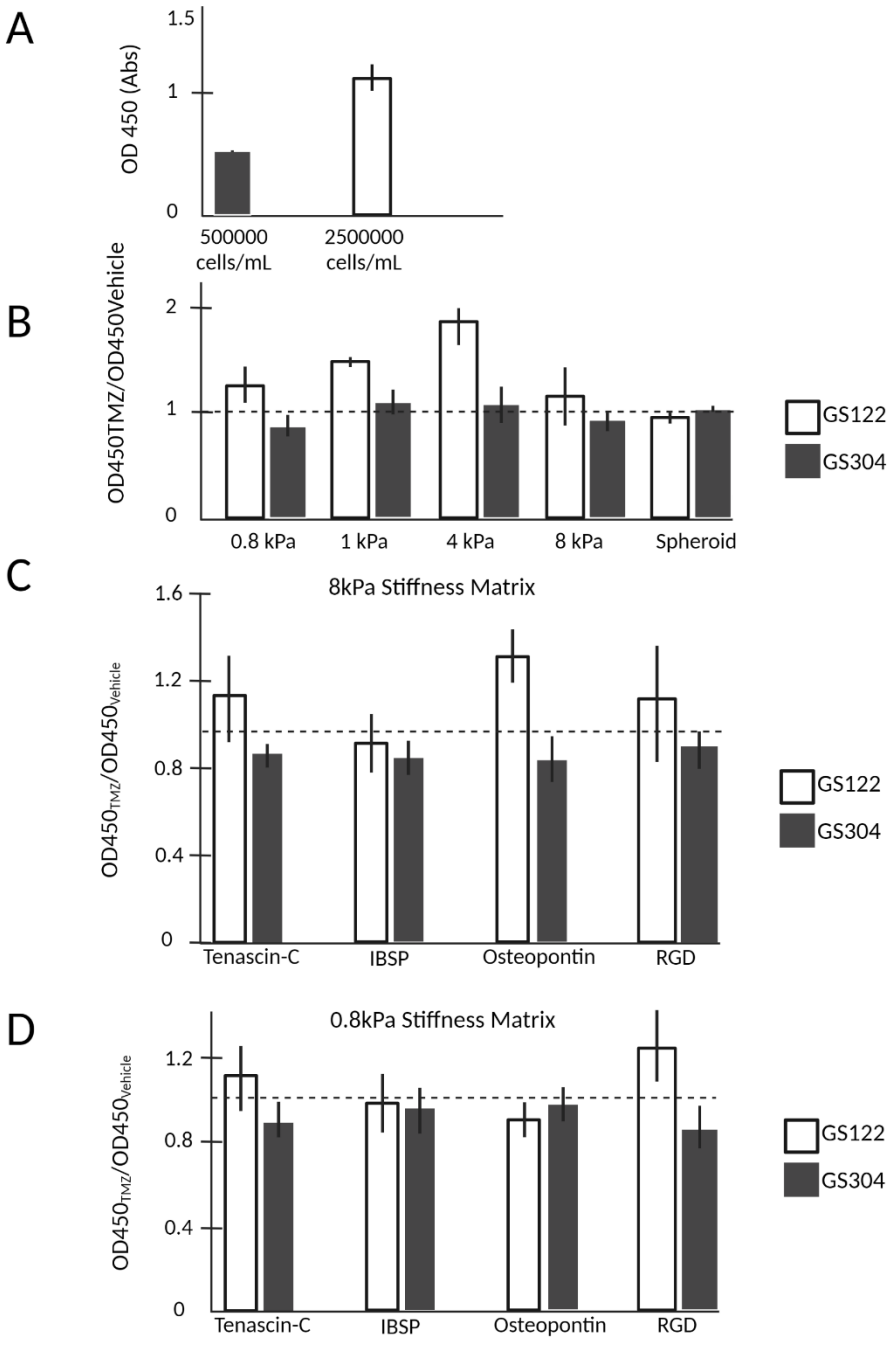
A
1.5
1
0
OD 450 (Abs)
500000 cells/mL
2500000 cells/mL
B
OD450TMZ/OD450Vehicle
2
1
0
0.8 kPa
1 kPa
4 kPa
8 kPa
Spheroid
GS122
GS304
C
8kPa Stiffness Matrix
OD450TMZ/OD450Vehicle
1.6
1.2
0.8
0.4
0
Tenascin-C
IBSP
Osteopontin
RGD
GS122
GS304
D
0.8kPa Stiffness Matrix
OD450TMZ/OD450Vehicle
1.2
0.8
0.4
0
Tenascin-C
IBSP
Osteopontin
RGD
GS122
GS304

Figure 3-3: Orthogonal presentation of stiffness and integrin-binding peptide reveals intrinsic biological differences between GBM cell lines.
(A) Typical absorbance values for GS122 cells encapsulated in a 10 μL hydrogel at a density of 500,000 or 2,500,00 cells per mL. (B) Drug response data for GS122 and GS304 cell lines are visualized by normalizing the OD450 value of the drug-treated wells (N = 5) by the average of the vehicle-treated wells (N = 5). Viability in the context of drug treatment was observed to vary nonlinearly for hydrogel stiffness, demonstrating variation between cell lines. (C,D) Drug response data for GS122 and GS304 cell lines when the type of integrin-binding peptide was included and matrix stiffness was varied orthogonally. All error bars represent the 95% confidence intervals obtained from bootstrapping each condition by N = 10,000. The dashed line (y-axis = 1) corresponds to the case where OD450 for the treatment conditions equals the vehicle. All experimental values were obtained after seven days in culture; TMZ was added three days after initial encapsulation for drug studies.

3D hydrogel cultures can be visualized using standard light microscopy to assess how cell morphology and invasive behaviors are affected by culture conditions in a cell-line-dependent manner (**Figure 4**). Both GS122 and GS304 cells spread when cultured in soft or stiff hydrogel matrices, including RGD-containing peptides **(Figure 4A)**. While peptides affected cell spreading, the ability of a cell to spread did not necessarily predict the ability of the culture to acquire TMZ resistance. For example, GS122 cells show a similar lack of spreading in both 0.8 and 8 kPa with osteopontin; however, GS122 only showed enhanced resistance to TMZ in the 8 kPa condition (**Figure 4B**). Finally, this miniaturized, 3D culture platform can be used to culture human cells from other tumor types, including viable organoids of terminally differentiated, neuroendocrine prostate cancer cells (**Figure 4C**).

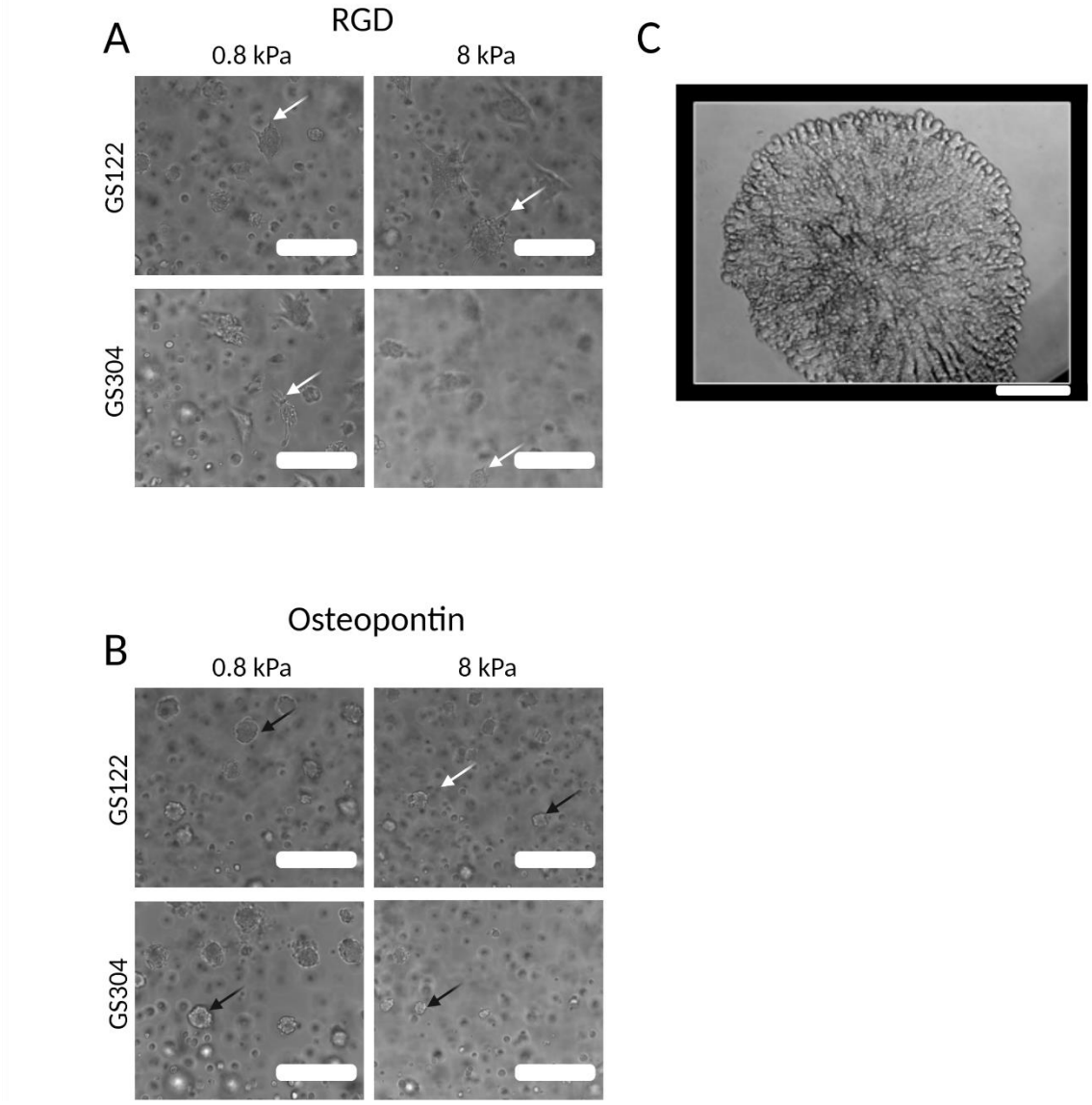

Figure 3-4: Morphological differences between cells encapsulated in different HA-based hydrogel environments.

(A) Phase-contrast images of GS122 and GS304, when cultured in a hydrogel (0.8 and 8 kPa), displayed an RGD motif. White arrows indicate cells with spread morphologies. (B) Phase images of GS122 and GS304, when cultured in a hydrogel (0.8 and 8kPa), displayed a peptide

derived from osteopontin. White arrows indicate cells with spread morphologies. Black arrows indicate cells with rounded morphologies. After seven days in culture, images were taken, and TMZ was added three days after initial encapsulation. (C) Phase image of a terminally differentiated neuroendocrine prostate organoid. Scale bars = 200 μm (for A,B); 100 μm (for C).

Protein	Peptide Sequence
RGD	GCGYGRGDSPG
Tenascin-C	GCGYGRSTDLPGLKAATHYTITIRGV
Integrin-binding sialoprotein (IBSP)	GCGYGGGGNGEPRGDTYRAY
Osteopontin	GCGYGTVDVPDGRGDSLAYG

Table 3-1: ECM proteins and derived peptide sequences.

Reagent	Initial Concentration	Volume (μL)	Final Concentration
HA-SH Solution	10 mg/mL	2300	5 mg/mL
PEG-SH	100 mg/mL	503	Varies per experiment
PEG-Norbornene	100 mg/mL	443	Varies per experiment
Peptide	4 μM	288	.250 μM
LAP	4 mg/mL	288	.25 mg/mL
HEPES-HBSS	N/A	798	

Table 3-2: Typical final formulation components for hydrogel.

Variable	Parameter
F	Force
E	Young's Modulus
ν	Poissons's Ratio
δ	Indentation (vertical tip position)
a	Radius of contact circle
R_S	Radius of Sphere

Table 3-3: Variables and corresponding parameters for AFM calculations.

3.7. DISCUSSION:

The current work presents methods to generate 3D, miniaturized cultures within HA-based while simultaneously altering matrix stiffness and peptides available for integrin engagement. This technique enables the systematic study of how matrix parameters affect cellular phenotypes (e.g.,

the viability of cancer cells exposed to chemotherapy) with increased throughput. Previous approaches, including that presented herein, have tuned hydrogel stiffness by varying the percent total polymer in the final formulation, where stiffer hydrogels have a higher polymer content[21,31]. However, this approach necessitates preparing a unique hydrogel formulation for each stiffness desired, a process that intrinsically lowers throughput. Here, hydrogel stiffness is tuned by varying UV irradiance during crosslinking so that hydrogels of multiple stiffnesses can be obtained from a single precursor solution. Future practitioners who may not have the opportunity to construct the custom illuminator described here can easily substitute a commercially available UV spot-curing device and adjust illumination as different sectors of a well plate are cured. The downside to using a commercial spot-curing device is decreased throughput compared to the custom illuminator. A limitation of the current methods is that unique solutions must still be prepared for each peptide condition. Similar methods have been used previously by other groups to produce stiffness-gradient-containing hydrogels[37,38]. However, this study demonstrates how photocrosslinking can enable the miniaturization of experimental samples and reduce the complexity of experimental setups. Overall, these improvements will allow researchers to increase experimental throughput when conducting 3D cultures in matrix-mimetic biomaterials and have utility across several fields in biomedical science beyond neuro-oncology.

The representative results demonstrate how this technique can be used to set up miniaturized, 3D cultures of patient-derived GBM cells in defined matrices, in which available integrin-binding peptides and stiffnesses are varied, within a standard 384-well plate appropriate for several standard assays. This method presents representative results to screen how matrix parameters

affect responses to TMZ chemotherapy in GBM cells derived from two unique patients, denoted as GS122 and GS304 cells. Of the two patient-derived cell lines evaluated here, the response of GS122 cells to TMZ treatment was sensitive to the matrix microenvironment, while that of GS304 cells was insensitive. Regarding matrix stiffness, GS122 cells cultured in 3D hydrogels with a 4 kPa micro-compressive modulus maximized TMZ resistance, under which condition treated cells increased in number more than untreated cells over a 7-day experimental course. Mechanical properties had larger effects on TMZ resistance than the integrin-binding peptides included. Thus, it is expected that the impact of varying peptide concentrations, alone and in combination, will enable the discovery of matrix conditions promoting drug resistance in the future. The insensitivity of GS304 cells to their surrounding matrix may indicate that the matrix is more influential on cells, like GS122 cells, that are originally sensitive to TMZ yet acquire resistance during treatment. In contrast, the extent to which matrix cues affect cells that are already treatment-resistant at the beginning of the experiment is unclear, as with GS304 cells.

Results from this study deviated somewhat from previously reported results. The softest HA-based hydrogels evaluated (1 kPa bulk Young's modulus, mimicking the stiffness of native brain) promoted maximal TMZ resistance GBM cells derived from four tumors from different patients than that evaluated here[21]. There are several possible reasons for this discrepancy. First, an expanded range of hydrogel stiffnesses was interrogated in the current study, which compared hydrogels across a range of 0.8 kPa to 8 kPa micro-compressive moduli, while previous studies compared only hydrogels with 1 kPa and 2 kPa Young's moduli. Additionally, in the previous studies, mechanical characterization was done at the bulk scale using linear mechanical

compression to estimate Young's modulus, whereas, in this study, AFM was used to measure a micro-compressive modulus. For researchers seeking to implement the methods present here who do not require micro-scale mechanics measurements, bulk scale moduli, using rheometry or linear mechanical testing, are perfectly acceptable substitutes for AFM. Notably, micro-mechanical analyses revealed the heterogeneous moduli across the surface of a single gel. Comparable AFM measurements on the hydrogels formulated in previous studies have not been made, but it is expected that the variance of stiffnesses presented within a single hydrogel to have been greater than those in the current study. Hydrogels in the previous studies were generated using a Michael-type addition crosslinking reliant on kinetic mixing at 37 degrees C[10,21,24]. In contrast, photocrosslinking permits thorough mixing of hydrogel precursors prior to light exposure, which improves homogeneity within the 3D hydrogel and, in turn, reduces the variability of cell responses. Finally, GBM tumors exhibit notoriously heterogeneous and unpredictable behavior[39] and, thus, it is reasonable to expect that cells derived from individual tumors would likewise have unique properties. This lack of consistency across patient samples motivates the need for a high-throughput platform for elucidating patient-specific tumor characteristics.

Common pitfalls when performing the miniaturized hydrogel photocrosslinking procedure include incomplete mixing of hydrogel precursors, resulting in poor reproducibility, and spontaneous gelation of the HA solution while mixing. These issues can be mitigated by stirring the HA-thiol for a minimum of 45 min and the complete precursor solution for at least an additional 30 min while closely monitoring the pH of hydrogel precursor solutions to ensure it

remains below 7 to prevent thiol oxidation and formation of disulfide to crosslinks. In contrast to crosslinking methods using a kinetic Michael-type addition mechanism[10,21], the photocrosslinking method used in this protocol lowers the probability of spontaneous gelation when all reagents are combined[21]. Quality control checkpoints are highly recommended, such as measuring HA thiolation percentage[31] and making extra hydrogels for parallel mechanical testing to each batch of 3D cultures. Finally, seeding densities for 3D encapsulation in hydrogels need to be identified for each cell type or line used. Generally, the results show that a minimum concentration of 1 million cells/mL is sufficient for the 3D culture of most cells, which form spheroids, including patient-derived GBM cells, human embryonic stem cells (H9), and human-induced pluripotent stem cells (data not shown). The inclusion of ROCK inhibitor treatment prior to encapsulation (step 4.1) when using particularly sensitive cells is also recommended[40].

In the context of developing new treatment approaches for GBM, the protocol presented here provides methods for functionally screening drug responses of patient-derived GBM cells within a physiologically relevant microenvironment. A rich repository of genetic, epigenetic, and clinical mRNA expression data for GBM (and other cancers) is publicly available thanks to the efforts of The Cancer Genome Atlas (TCGA) and others[15]. Used in conjunction with these large datasets, it is expected that data generated from functional screens of miniaturized, 3D cultures can reveal new correlations, improving the prediction of clinical outcomes in individual patients. For example, subpopulations of patient tumors may be identified for which some treatment, for example, matrix-disrupting compounds such as cilengitide, may improve clinical outcomes[41]. In addition to drug response, this culture platform enables assessments of tumor cell invasion using

well-plate compatible, high-content imagers. The flexibility of this platform to incorporate many different peptides, alone or in combination, while orthogonally varying stiffnesses may help identify matrix features driving GBM tumor aggression.

Beyond GBM, these methods can be adapted to investigate the effects of matrix parameters on other cell types in the context of other diseases, tissue development, and normal tissue function. In the future, it will be straightforward to increase the throughput of these methods further, as they have been specifically designed to be performed in the context of multi-well plates to facilitate adoption into existing workflows for drug discovery by utilizing commercially available automated liquid handlers and high-content imagers. Facile integration with existing infrastructure and increased automation, which decreases the technical skills required to produce and maintain cell-laden, 3D hydrogel cultures, will significantly lower barriers to adopting this method. While the work here specifically presents cultures within HA-based hydrogels, it is expected that this method can be easily translated to other commonly used photocrosslinkable materials for 3D cell culture, such as methacrylated gelatin, and that the methods reported here will provide a helpful guideline for additional applications.

3.8. ACKNOWLEDGMENTS:

The authors would like to specifically acknowledge Carolyn Kim, Amelia Lao, Ryan Stoutamore, and Itay Solomon for their contributions to earlier iterations of the photogelation scheme. Cell lines GS122 and GS304 were generously provided by David Nathanson. All figures were created with BioRender.com. UCLA core facilities, the Molecular Screening Shared

Resources, and the Nano and Pico Characterization Laboratory were instrumental to the work. Chen Chia-Chun was supported by the UCLA Eli and Edythe Broad Center of Regenerative Medicine and Stem Cell Research Training Program. Grigor Varuzhanyan was supported by a Tumor Cell Biology Training Program NIH Grant (T32 CA 009056).

3.9. DISCLOSURES:

The authors have nothing to disclose.

3.10. REFERENCES:

1. Scannell, J. W., Blanckley, A., Boldon, H., Warrington, B. Diagnosing the decline in pharmaceutical R&D efficiency. *Nature Reviews Drug Discovery*. **11** (3), 191–200 (2012).

2. Waring, M. J. et al. An analysis of the attrition of drug candidates from four major pharmaceutical companies. *Nature Reviews Drug Discovery*. **14** (7), 475–486 (2015).

3. Khozin, S., Liu, K., Jarow, J. P., Pazdur, R. Why do oncology drugs fail to gain US regulatory approval? *Nature Reviews Drug Discovery*. **14** (7), 450–451 (2015).

4. Booth, B., Ma, P., Glassman, R. Oncology's trials. Market indicators. *Nature Reviews Drug Discovery*. **2** (8), 609–610 (2003).

5. Da Ros, M. et al. Glioblastoma chemoresistance: The double play by microenvironment and blood-brain barrier. *International Journal of Molecular Sciences*. **19** (10), 2879 (2018).

6. Broekman, M. L. et al. Multidimensional communication in the microenvirons of glioblastoma. *Nature Reviews Neurology*. **14** (8), 482–495 (2018).

7. Grundy, T. J. et al. Differential response of patient-derived primary glioblastoma cells to environmental stiffness. *Scientific Reports*. **6** (1), 1–10 (2016).

8. Gomez-Roman, N., Stevenson, K., Gilmour, L., Hamilton, G., Chalmers, A. J. A novel 3D human glioblastoma cell culture system for modeling drug and radiation responses. *Neuro-Oncology*. **19** (2), 229–241 (2017).

9. Simoni, R. D. et al. Basement membrane complexes with biological activity. *Biochemistry*. **25** (2), 312–318 (2002).

10. Xiao, W. et al. Brain-mimetic 3D culture platforms allow investigation of cooperative effects of extracellular matrix features on therapeutic resistance in glioblastoma. *Cancer Research*. **78** (5), 1358–1370 (2018).

11. Aisenbrey, E. A., Murphy, W. L. Synthetic alternatives to Matrigel. *Nature Reviews Materials*. **5** (7), 539–551 (2020).

12. Spinelli, C. et al. Molecular subtypes and differentiation programmes of glioma stem cells as determinants of extracellular vesicle profiles and endothelial cell-stimulating activities. *Journal of Extracellular Vesicles*. **7** (1), 1490144 (2018).

13. Ostrom, Q. T., Cioffi, G., Waite, K., Kruchko, C., Barnholtz-Sloan, J. S. CBTRUS statistical report: Primary brain and other central nervous system tumors diagnosed in the United States in 2014–2018. *Neuro-Oncology*. **23** (Supplement_3), iii1–iii105 (2021).

14. Stupp, R. et al. Radiotherapy plus concomitant and adjuvant temozolomide for glioblastoma. *New England Journal of Medicine*. **352** (10), 987–996 (2005).

15. Brennan, C. W. et al. The somatic genomic landscape of glioblastoma. *Cell*. **155** (2), 462–477 (2013).

16. Tomczak, K., Czerwińska, P., Wiznerowicz, M. The Cancer Genome Atlas (TCGA): An immeasurable source of knowledge. *Contemporary oncology (Poznan, Poland)*. **19** (1A), A68–A77 (2015).

17. Lee, S. Y. Temozolomide resistance in glioblastoma multiforme. *Genes and Diseases*. **3** (3), 198–210 (2016).

18. Joo, K. M. et al. Patient-specific orthotopic glioblastoma xenograft models recapitulate the histopathology and biology of human glioblastomas in situ. *Cell Reports*. **3** (1), 260–273 (2013).

19. Levy, N. The use of animal as models: Ethical considerations. *International Journal of Stroke*. **7** (5), 440–442 (2012).

20. Phon, B. W. S., Kamarudin, M. N. A., Bhuvanendran, S., Radhakrishnan, A. K. Transitioning preclinical glioblastoma models to clinical settings with biomarkers identified in 3D cell-based models: A systematic scoping review. *Biomedicine & Pharmacotherapy*. **145**, 112396 (2022).

21. Xiao, W. et al. Bioengineered scaffolds for 3D culture demonstrate extracellular matrix-mediated mechanisms of chemotherapy resistance in glioblastoma. *Matrix Biology*. **85–86**, 128–146 (2020).

22. Brancato, V., Oliveira, J. M., Correlo, V. M., Reis, R. L., Kundu, S. C. Could 3D models of cancer enhance drug screening? *Biomaterials*. **232**, 119744 (2020).

23. Xu, X., Farach-Carson, M. C., Jia, X. Three-dimensional in vitro tumor models for cancer research and drug evaluation. *Biotechnology Advances*. **32** (7), 1256–1268 (2014).

24. Xiao, W., Ehsanipour, A., Sohrabi, A., Seidlits, S. K. Hyaluronic-acid based hydrogels for 3-dimensional culture of patient-derived Glioblastoma Cells. *Journal of Visualized Experiments: JoVE*. **138**, e58176 (2018).

25. Preston, M. Digestion products of the PH20 hyaluronidase inhibit remyelination. *Annals of Neurology*. **73** (2), 266–280 (2013).

26. Kim, Y., Kumar, S. CD44-mediated adhesion to hyaluronic acid contributes to mechanosensing and invasive motility. *Molecular Cancer Research*. **12** (10), 1416–1429 (2014).

27. Pibuel, M. A., Poodts, D., Díaz, M., Hajos, S. E., Lompardía, S. L. The scrambled story between hyaluronan and glioblastoma. *The Journal of Biological Chemistry*. **296**, 100549 (2021).

28. Xiao, W., Sohrabi, A., Seidlits, S. K. Integrating the glioblastoma microenvironment into engineered experimental models. *Future Science OA*. **3** (3), FSO189 (2017).

29. Trombetta-Lima, M. et al. Extracellular matrix proteome remodeling in human glioblastoma and medulloblastoma. *Journal of Proteome Research*. **20** (10), 4693–4707 (2021).

30. Schregel, K. et al. Characterization of glioblastoma in an orthotopic mouse model with magnetic resonance elastography. *NMR in Biomedicine*. **31** (10), e3840 (2018).

31. Xiao, W., Ehsanipour, A., Sohrabi, A., Seidlits, S. K. Hyaluronic-acid based hydrogels for 3-dimensional culture of patient-derived glioblastoma cells. *Journal of Visualized Experiments: JoVE*. (138), 58176 (2018).

32. Guz, N., Dokukin, M., Kalaparthi, V., Sokolov, I. If cell mechanics can be described by elastic modulus: Study of different models and probes used in indentation experiments. *Biophysical Journal*. **107** (3), 564–575 (2014).

33. Sneddon, I. N. The relation between load and penetration in the axisymmetric boussinesq problem for a punch of arbitrary profile. *International Journal of Engineering Science*. **3** (1), 47–57 (1965).

34. Soofi, S. S., Last, J. A., Liliensiek, S. J., Nealey, P. F., Murphy, C. J. The elastic modulus of Matrigel™ as determined by atomic force microscopy. *Journal of Structural Biology*. **167** (3), 216–219 (2009).

35. Mayerhöfer, T. G., Popp, J. Beer's law - Why absorbance depends (almost) linearly on concentration. *Chemphyschem: A European Journal of Chemical Physics and Physical Chemistry*. **20** (4), 511–515 (2019).

36. Puth, M. T., Neuhäuser, M., Ruxton, G. D. On the variety of methods for calculating confidence intervals by bootstrapping. *Journal of Animal Ecology*. **84** (4), 892–897 (2015).

37. Lavrentieva, A. Gradient hydrogels. *Advances in Biochemical Engineering/Biotechnology*. **178**, 227–251 (2020).

38. Zhu, D., Trinh, P., Li, J., Grant, G. A., Yang, F. Gradient hydrogels for screening stiffness effects on patient-derived glioblastoma xenograft cellfates in 3D. *Journal of Biomedical Materials Research. Part A*. **109** (6), 1027–1035 (2021).

39. da Hora, C. C., Schweiger, M. W., Wurdinger, T., Tannous, B. A. Patient-derived glioma models: From patients to dish to animals. *Cells*. **8** (10), 1177 (2019).

40. Li, W. et al. Characterization and transplantation of enteric neural crest cells from human induced pluripotent stem cells. *Molecular Psychiatry*. **23** (3), 499–508 (2018).

41. Scaringi, C., Minniti, G., Caporello, P., Enrici, R. M. Integrin inhibitor cilengitide for the treatment of glioblastoma: A brief overview of current clinical results. *Anticancer Research*. **32** (10), 4213–4224 (2012).

Chapter 4. Investigating solute diffusivity in hyaluronic acid-based hydrogels

4.1. Introduction

Cellular models started as 2D cultures on glass which allowed for the culture and growth of cells in real time and allowing for the characterization of cells.[1] In comparison to the 2D cultures commonly present in lab, the in vivo environment features an extra level of dimensionality and other effects associated with having an extracellular matrix.[2] Models which extend into the third dimension correspondingly increase the complexity of the system and require additional characterization to aid in the interpretation of biological phenomenon.

In the works reported in this dissertation Chapter 3 covered the fabrication of 3D hyaluronic acid (HA) based hydrogels for the culture of patient derived glioblastoma (GBM) cultures. In that chapter, we utilized atomic force microscopy (AFM) to provide a relevant cell scale characterization of the local elasticity of hydrogel.

The high resolution afforded by AFM enabled us to assess the heterogeneity in hydrogel architecture of our HA based hydrogel which was anticipated given the stochastic nature of photo crosslinking employed. Indeed, techniques utilizing probes embedded throughout hydrogel matrices have revealed stunning levels of heterogeneity in local polymer network architecture.[3] Given the cellular scale on the order of microns, additional methods which can characterize hydrogel environments at the micron scale will be helpful in identifying the mechanisms by which cellular activities are influenced by their local environment.

In a cellular context, diffusion of growth factors, nutrients, oxygen, waste, and larger molecules such as extracellular vesicles are known to greatly affect cellular activity.[4] Thus, understanding how components of the physical microenvironment affect the transport of these factors is of great

interest for both biological and pharmacological means. For example, the capacity of the blood brain barrier to selectively filter based on size and charge places a restriction on the chemical nature of therapeutics that can be effectively delivered to the CNS .[5] The inability to achieve penetration to the CNS has been a barrier to therapeutic development for GBM.

Hydrogels as being comprised of largely water and formed by the crosslinking of polymer networks provide a useful model for studying hindered solute diffusion.[6] The diffusion of molecules in a hydrogel environment is known to be affected by the physical properties of hydrogels eg. stiffness. Like *in vivo reports,* gradients of growth factors and other signaling molecules have been shown to affect the biology of encapsulated cells in several reports.[7,8] Additionally, hydrogels are a popular vehicle for drug delivery applications and has accumulated a rich literature of reports on methods to characterize and utilize hydrogels to study diffusion.[9–16] Beyond these application, the emergence of extracellular vesicles as a major player in cell-cell communication as well as reports characterizing their activity as a function of size there is a greater need to have means to quantify the effect of porosity of hydrogel constructs on mass transport.[17–19]

The methods to validate the predicted mesh size of hydrogels have generally been limited by the fact that the most direct measurements of mesh size, electron microscopy, requires the dehydration of samples and thereby characterize them outside of physiologically relevant environments.[20] Thus, indirect techniques which measure effective diffusivity of molecules in hydrated systems have been developed.[4,21] More precise methods may utilize nuclear magnetic resonance to directly probe the hydrated portions of the network and typically require more advanced setup and expertise to interpret.[22] A more accessible technique is Fluorescence

Recovery after Photobleaching (FRAP), which estimates the diffusivity of a fluorescently tagged molecule through measuring the time it takes for a cylindrical photobleached region to return to a steady state level of fluorescence.[4] This technique can be performed with several preparations of fractionated fluorescently labeled dextran molecules to determine a "molecular weight cutoff" for which diffusivity of the labeled molecules decreases, and the hydrodynamic radii of those species can be used as a rough estimate of the mesh size of the hydrogel.[23,24] Commercial preparations of these molecules are commonly characterized by either their weight average Molecular weight (M_w) or number average molecular weight (M_n) as well as their polydispersity index (M_w / M_n).

In previous publications, we utilized FRAP and other diffusivity measurement techniques to characterize our hydrogels.[25–27] However, unlike previous reports and methodologies, we were unable to determine molecular weight cutoffs as our higher M_w FITC-dextrans would always diffuse into our gels.[9] To address these inconsistencies in our FRAP data, we utilized SEC-MALS and DLS to determine the largest species capable of diffusing into a hydrogel as well as the distribution of species present in the hydrogel. The methods described in this chapter will prove helpful to individuals who are interested better understanding the effect of hydrogel network architecture on mass transport.

4.2. Materials and Methods

Fabrication of hydrogels

Photogels were prepared as described previously (chapter 2), in brief crosslinking densities of hyaluronic acid hydrogels were varied by altering the total polymer content of 4-arm thiol terminated PEG while maintaining a 1:1.2 molar ratio of thiol moieties to norbornene moieties.

Total thiol concentration for formulations tested in this manuscript were used as described previously.[28] Hydrogels were crosslinked by exposure to 365 nm wavelength at 4.2 mW/cm^2 for 15 seconds. Final hydrogel stiffnesses used in this study were of 100 Pa, 250 Pa, 300 Pa, 700 Pa, and 1000 Pa storage modulus.

Infiltration and exfiltration of differently sized FITC dextrans

FITC labeled dextrans of various molecular weight averages (70 kDa, 150 kDa, 250 kDa,500 kDa) were infused into 80 µL HA based hydrogels by swelling HA-hydrogels with a 1 mg/mL solution of FITC-dextran in PBS overnight at room temperature. The next day, loading of FITC-Dextrans into gels was visually confirmed by inspecting individual gels. FITC-Dextrans were exfiltrated from gels by placing them back into 100 µL of PBS for overnight extraction at room temperature. The next day exfiltrate solutions were isolated from each gel.

Size exclusion chromatography multi angle light scattering

Exfiltrates from HA based hydrogels infused with 70 kDa and 150 kDa FITC-Dextran were filtered with a .22 µm syringe filter. These solutions were then injected into a wyatt sec column with feature size 5 µm and 300 angstroms. Following fractionation, sample entered a wyatt minidawn multi angle light scattering system and an attached optilab rEX. A maximum flow rate of .1mL/min^2 was specified. Sample buffer consisted of PBS while storage buffer was composed of ultra-pure water. Both solutions were sterile filtered with a .22 µm filter and degassed under vacuum. An aktapure machine was used to control flow rates and sample injection. 70 kDa and 150 kDa FITC dextran at 20 mg/mL was used for reference runs. BSA standard was prepared at 5 mg/mL and filtered with a .22 µm filter to remove clumps. All data analysis was performed with Astra 6.

Flouresence Recovery after Photobleaching

Following incubation with 150 kDa or 500 kDa weight average fluorescein isothiocyanate-dextran (FITC-D) diluted to 1 mg/mL in PBS overnight at 37 degrees C. Infused hydrogels were interrogated by the 488 laser line on an SP5 laser scanning confocal microscope (Leica) for image acquisition and photobleachingbleaching. Images were recorded prior to photobleach (5 frames) and after photobleach (1000 frames) at 10% laser power. For photobleaching, a 30 µm diameter ROI was photobleached by exposure to 100% laser power for 20 seconds. Resulting fluorescence recovery graphs were plotted and t_d determined by calculating the time it took for flouresence to recover to its half maximum. Effective diffusivity coefficients(D_e) were calculated using a simplified Fick's law.[29]

Dynamic light scattering

Exfiltrates from hydrogels infused with 70 kDa and 250 kDa were sterile filtered with .22 µm filters and loaded into low volume cuvettes. Distributions of exfiltrates or 5 mg/mL reference solutions were determined by photon correlation spectroscopy using a zetasier nano. A PBS dispersant was used and material RI set at 1.48. Measurements were carried out at 25 degrees Celsius with a light-scattering detection angle of 173 degrees. Measurement position was set at 3 mm and attenuator setting was set using the automated algorithm built into the machine. Frequency and undersize curves were generated using Number PSD analysis. For centrifugation fractionation a 50 kDA molecular weight cut off (MWCO) column was used to filter the 70 kDA and 250 kDA reference solutions. The proportion of the solutions which passed through the column are referred to as the 'small' fraction while the portion that failed to travel through the column was resolubilized with PBS and referred to as the 'large' fraction.

4.3. Results

Fluorescence Recovery after Photobleaching of HA based hydrogels overestimates effective diffusivity constants at high molecular weights

Our study was prompted by observations we had in examining high molecular weight FITC-dextran diffusion through HA-based hydrogels using FRAP. As porosity of hydrogels are intrinsically tied to the stiffness of HA-based hydrogels, we used FITC-dextrans as models for the diffusion of molecules of similar size scale. Strangely, we found that contrary to our intuition that effective diffusivity of 150 kDa FITC-dextran was lower than the diffusivity of larger 500 kDa FITC-dextran (Figure 1A). Closer inspection of our recovery curves (Figures 1B and 1C) revealed that although the half time recovery constant of the two curves was indeed similar, and thus yielded equal diffusivity constants. However, the relative fluorescent intensities of the hydrogel region between the two curves revealed a partitioning effect wherein the concentration of higher molecular weight FITC-Dextran was lower in the hydrogel region. This 'partitioning' effect has been described previously in other reports confirming our suspicions that our diffusion coefficient discrepancies were not a unique problem and in fact were frequently a nuisance as they restricted calculation of diffusivity coefficients.[30,31] We hypothesized that the driving force behind this partitioning effect was the inability of higher molecular weight FITC-dextran species to diffuse into our HA hydrogel matrix and that characterization of the fraction of FITC-dextran species that were capable of diffusing into the hydrogel would indirectly provide measurements of the largest pore size in the hydrogel matrix.

A

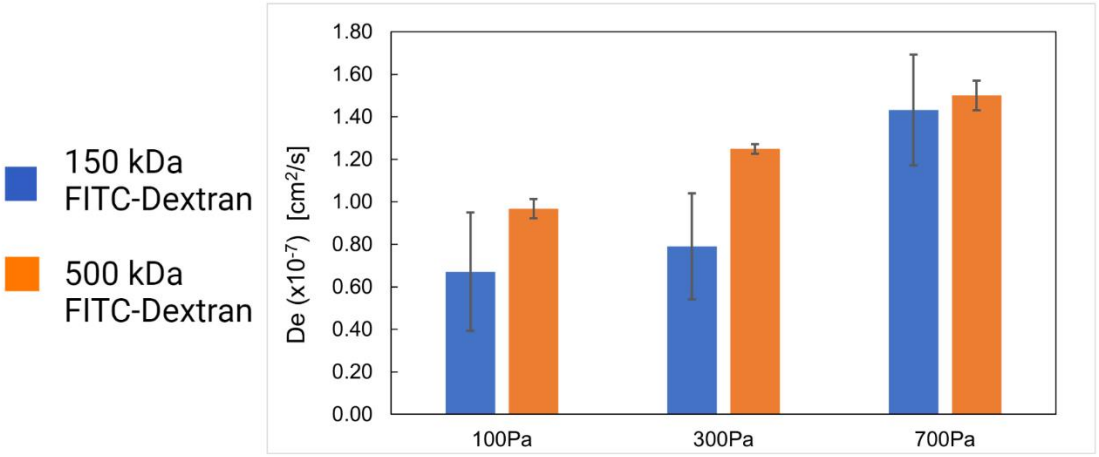
150 kDa FITC-Dextran
500 kDa FITC-Dextran
De (x10-7) [cm2/s]
1.80
1.60
1.40
1.20
1.00
0.80
0.60
0.40
0.20
0.00
100Pa
300Pa
700Pa

B

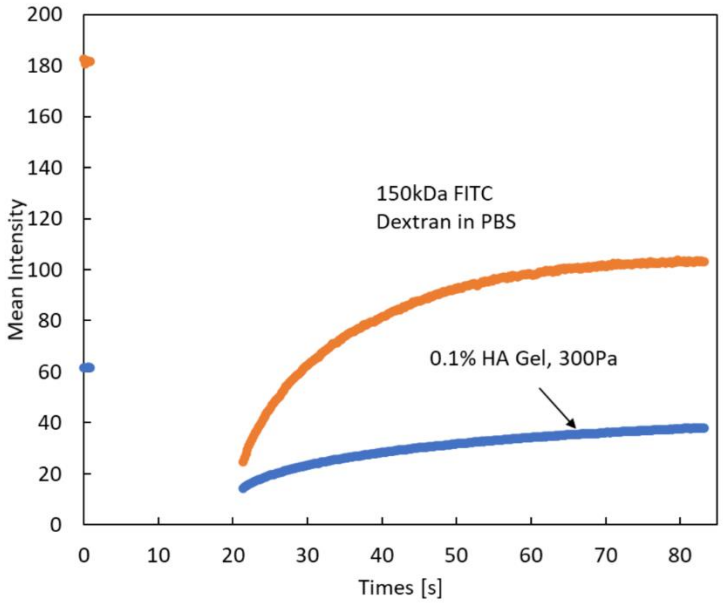
Mean Intensity
150kDa FITC Dextran in PBS
0.1% HA Gel, 300Pa
Times [s]

C

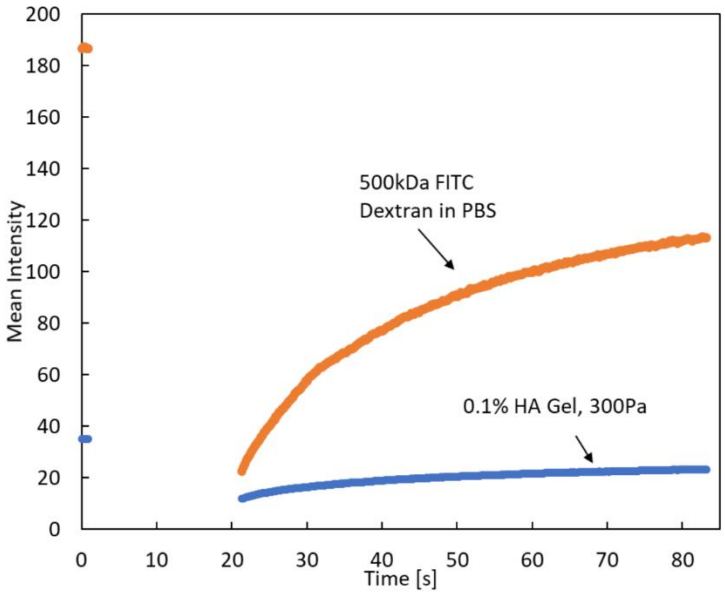
Mean Intensity
500kDa FITC Dextran in PBS
0.1% HA Gel, 300Pa
Time [s]

Figure 4-1: FRAP measurement reveal partitioning effect of dextrans in hydrogels
1A: Calculated Diffusion coefficients from FRAP experiments using hydrogels of storage moduli 100, 300 and 700 Pa. Error bars represent standard deviation taken from 6 pooled measurements of 2 hydrogels.

1B: Representative FRAP recovery curve from a 300 Pa storage modulus gel and 150 kDa FITC-Dextran. Note the difference in relative intensity between PBS (orange) and hydrogel (blue).

1C: Representative FRAP recovery curve from a 300 Pa storage modulus gel and 500 kDA FITC-Dextran. Note the difference in relative intensity between PBS (orange) and hydrogel (blue).

Size exclusion chromatography – Multi-angle Light Scattering (SEC-MALS) reveal stiffness dependent molecular weight cut offs for HA based hydrogels

To test our hypothesis that our discordant observations were due to differences between the molecular weights of FITC-dextran molecules present inside the hydrogel and the nominal weight of the FITC- dextran preparations we needed to interrogate the fraction of FITC-Dextran species inside the hydrogel. To isolate the fraction of interest, we infused the hydrogels with FITC-dextran as we would routinely do for a FRAP measurement. The following day, we replaced the FITC-dextran infusion solution with fresh PBS and incubated overnight to allow the infiltrated FITC-dextran species to reestablish equilibrium by diffusion out of the gel. The surrounding solution could then be easily collected and analyzed (Figure 2A). SEC-MALS is commonly used to characterize the sizes of FITC-dextran solutions that are commercially available.[32] We used this technique to now probe the FITC-Dextran solutions that present inside the gel using the strategy discussed above. We verified correct calibration of our system including the SEC column, injection handler, and MALS components by measuring the

molecular weights of defined BSA preparations. SEC-MALS measurements utilize several assumptions regarding the geometry of the analyte as well as empirical measurements of the refractive index increment, and scatter intensity to calculate the size of an analyte that were obtained from a literature search.[32–35]

We observed classic monomeric, dimer, trimers of BSA with the correct weights indicating our machine was properly operating.[36] In contrast to monodisperse samples, two reference FITC-dextran solutions appear as a broad spectrum of differing molecular weights.[36] Lower molecular weight FITC-dextrans were used in this portion of the study to avoid potential issues with clogging of the size exclusion column compared to our previous FRAP experiments (Communication to the authors by core facility personnel). To our surprise the distributions of FITC-dextran were more disperse than reported by the manufacturer with a PDI of 1.2 for the 150 kDA FITC Dextran and a PDI of 2 for the 70 kDA FITC-dextran (Figure 2B). Having validated the capacity for the SEC-MALS measurement to quantify the sizes of FITC-dextrans in solution we then applied this technique to the exfiltrate of different stiffness HA hydrogels. We examined the FITC-dextran exfiltrate of hydrogels 100 Pa storage modulus and 700 Pa storage modulus after infusion with FITC-dextran of size 150 kDa. (Figures 2C and 2D) We made rough estimates of 350 kDa and 200 kDa as size cut-offs for the 100 and 700 Pa storage modulus gels, respectively. As our measurements approached the noise floor of the system, due to low concentrations of FITC-Dextran in the exfiltrate, instability in molecular weight size was apparent (Figure 2D). Nevertheless, these observations support our hypothesis that the partitioning effect observed in FRAP was due to size exclusion effects.

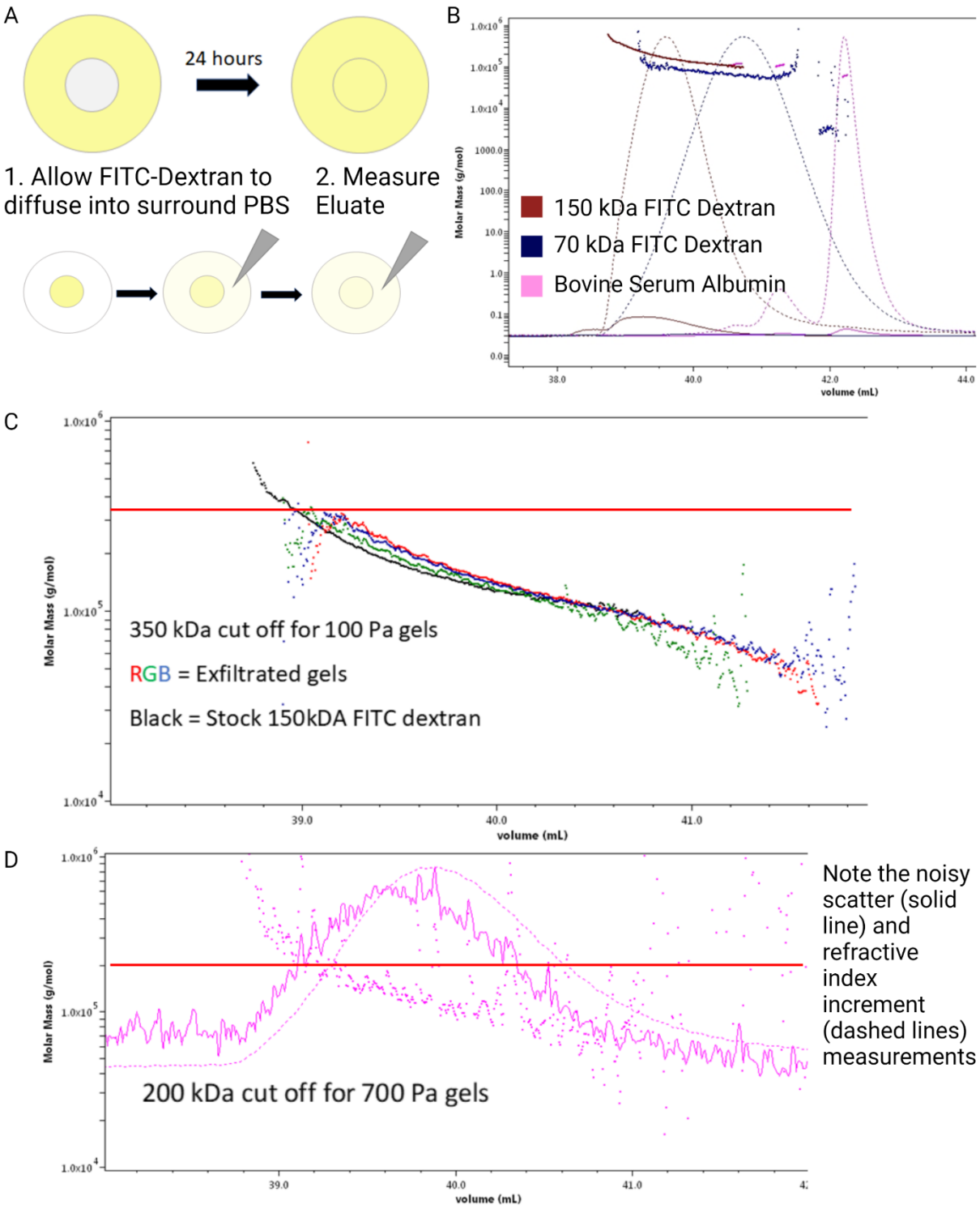

Note the noisy scatter (solid line) and refractive index increment (dashed lines) measurements

Figure 4-2: Size exclusion chromatography measurements identify dextran sizes in hydrogels
2A: Cartoon schematic of SEC-MALS measurement

2B: Validation of proper calibration of SEC-MALS machine by characterization of 20 mg/mL standards of FITC-Dextran and BSA

2C: Release profiles from 150 Pa Gels. Black line represents the reference population from figure 2A. Red, green, and blue samples represent three independent samples of 150 Pa storage modulus gels.

2D: Representative release profiles from ~1000 Pa storage modulus gel. Noisy measurements in the scatter, as well as refractive index increment channel lower confidence in predicted molecular weight cut off.

Interrogation of FITC-Dextran infiltrate by dynamic light scattering reveals shifts in molecular weight distributions of

Our results with SEC-MALS supported our hypothesis that differing distributions of molecular weights of FITC-dextrans can emerge due to the hydrogel acting as a molecular sieve and that this property is a consequence of the stiffness and network structure of the hydrogel. While our previous measurements elucidated the upper bound of particle sizes that can diffuse into the hydrogels, of more consequence to bulk measurements like FRAP is the underlying distribution of particles. An alternative approach to measurement of nanoparticles is dynamic light scattering (DLS), which in contrast to multi angle light scattering measures the scatter from a sample at one angle. This technique enables one to characterize the underlying distribution of particles as a function of their relative sizes by performing correlation analyses on speckle patterns.[37]

We investigated how stiffness of our hydrogel construct would affect the infiltration of FITC-dextran through DLS measurements. Using the same scheme depicted in Figure 2A we

characterized the eluate of FITC-dextrans which diffused out of the gel solutions using a low molecular weight FITC-dextran (70 kDa) and a high molecular weight FITC-dextran (250 kDa). Our previous of the 70 kDa FITC-Dextran with SEC-MALS suggested that very few if any particles were of a size greater than 200 kDa so we hypothesized that increasing the stiffness of our gels up to our stiffest formulations (1000 Pa) would have minimal effects on the distribution of FITC-dextrans capable of diffusing into the gel. Indeed, we found that there were minimal, if any, discernable effects on the size distribution of FITC-dextran particles in this group (Figure 3A). The appearance of a tail in the below 4 nm radius regime is possibly due to the combined effects of dilution from infiltration and exfiltration of the FITC-dextran into the hydrogel as well as removal of larger particles which can mask the presence of smaller particles.[38] We then examined the effect of hydrogel stiffness of gels with storage modulation on the softer spectrum of gels made and infiltrated in 250 kDa FITC-dextran. Although we did not have reference SEC-MALS characterization of this species we inferred based off the size distribution found in the 150 kDa FITC-dextran species that a significant portion of the FITC-dextrans would lie above the estimated 350 kDa molecular weight cut off. Indeed, all gels of stiffness 100 Pa, 250 Pa and 300 Pa demonstrated similar undersize curve profiles that differed drastically from the reference sample with 50 percent by number of particles appearing under 6 nm in diameter for gel exfiltrate samples while <5% of particles appearing for the reference sample. Given the propensity for higher molecular weight analytes to affect scatter signal more intensely in these measurements, it is possible that the movement of these presence of these smaller molecules are hidden by the larger particles (DLS citation).

A

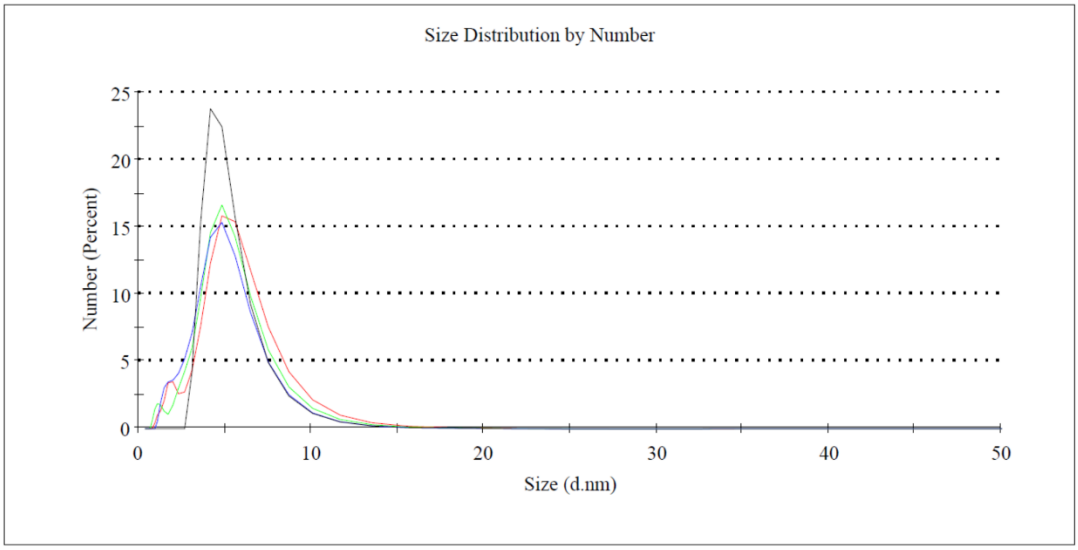

B

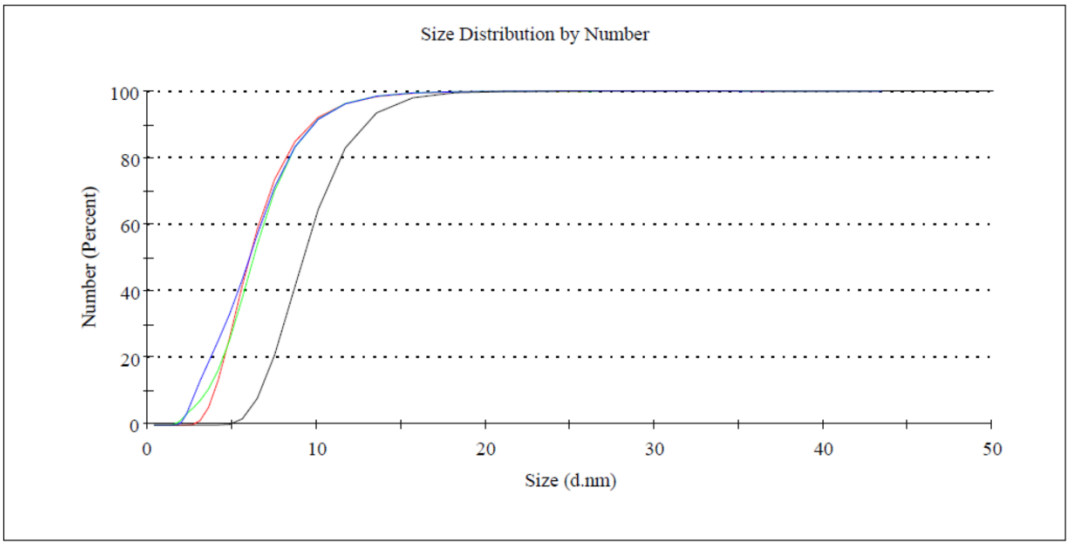

Figure 4-3: Dynamic light scattering measurements reveal distribution of particles diffusing into hydrogels.

3A: Frequency curve of the following samples. Black reference 70 kDa FITC-Dextran sample. Blue 350 Pa storage modulus gel, green 700 Pa storage modulus gel, red 1000 Pa storage modulus gel. Each sample is the average of three independent hydrogel infiltrates.
3B: Cumulative distribution function (Undersize Curve) of the following samples. Black: Reference 250 kDa FITC-Dextran. Blue: 150 Pa Storage Modulus. Green 250 Pa Storage Modulus. Red 350 Pa Storage modulus.

Molecular sieve nature of HA-based hydrogels confirmed by comparison to commercially available centrifuge fractionation columns

Taken together, this characterization of the FITC-dextran infiltrate suggests that the partitioning effect observed is due to hydrogels acting as a molecular sieve, thereby excluding FITC-Dextran molecules of larger sizes. We confirmed the molecular sieve nature of our hydrogels by comparing the distribution of FITC-dextran molecules capable of diffusing into our hydrogels with the distributions of FITC-dextrans emerging from fractionation using commercially available centrifugation columns with a nominal molecular weight cut off-of 50 kDa. As the 50 kDa MWCO was much lower than the average particle size in the 250 kDa FITC-dextran we saw that the number of particles appearing under 6 nm in diameter in the fractionated samples was even greater than the fraction appearing in the 150 Pa hydrogel condition (Figure 4A). While the general shape of the FITC-dextran populations from hydrogel and centrifuge column processed samples were similar, the wider distribution and longer tail found in the hydrogel sample is likely due to greater heterogeneity in the polymer network of our hydrogel. In contrast, when the 70 kDa FITC-dextran is fractionated by the 50 kDa centrifugation column a clear

separation is observed between the fractionated portions and the reference sample. Indeed, in this case because the distribution of the FITC-dextran reference (70 kDa) lies below the expected cut off value of the hydrogel we observe that the higher molecular weight tail of the hydrogel species matches that of the reference sample and differs from the fractionated sample. The appearance of a low molecular weight tail is once again presumably due to dilution effects.

A

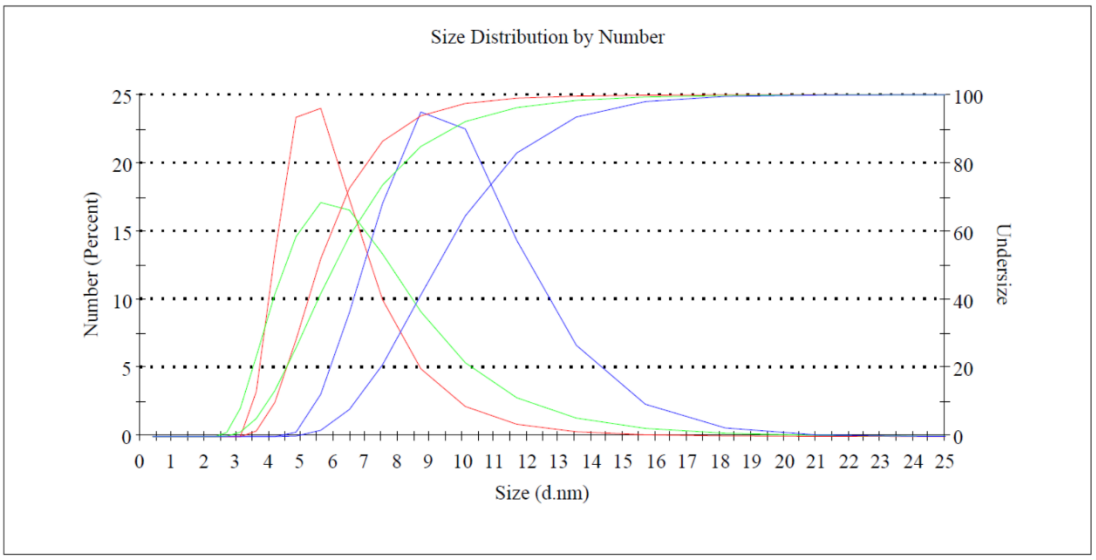

B

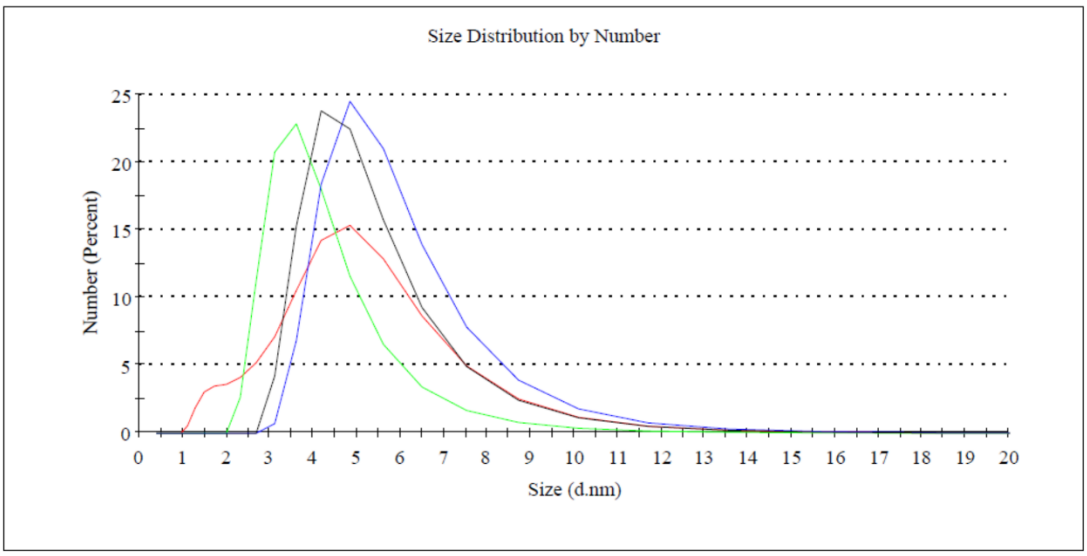

Figure 4-4: Hydrogels behave similarly to centrifuge fractionation columns.

4A: Combined frequency and undersize curves of Blue: Reference 250 kDa FITC dextran Red: Small fraction from 50 kDa MWCO centrifuge column, Green: 150 Pa storage modulus hydrogel.

4B: Frequency curve of Black: Reference 70 kDa FITC-Dextran, Red 1000 Pa hydrogel storage modulus hydrogel, Green: Small fraction from 50 kDa MWCO centrifuge column, Blue: Large fraction from 50 kDa MWCO centrifuge column.

4.4. Discussion

In this work we provide evidence suggesting that the partition effect noted to occur when performing FRAP experiments with FITC-dextrans is due to a size exclusion effect exhibited by hydrogels. The resulting characterization efforts consequently provide the methodology to estimate a molecular weight cut off metric using SEC-MALS and characterize the effect of this MWCO on FITC-Dextran diffusion by comparing the resulting distributions to distributions fractionated using commercially available fractionation columns.

Limitations in sample diluteness introduce a degree of uncertainty in the determination of an "absolute" molecular weight cut off size for the hydrogels tested but provide estimations that may be useful. On the other hand, as noted in figures 4B and 3A dilution effects by the infiltration and exfiltration steps may help elucidate the contribution of smaller molecular weight species that are normally masked by larger molecular weight analytes.

In this study, FITC-Dextrans were used in the context of a negatively charged hydrogel (hyaluronic acid) which introduces electrostatic interactions that will affect both partitioning and diffusion. Indeed, in certain hydrogel applications electrostatic interactions are utilized to limit the diffusion of smaller species.[11] An exciting avenue to further develop this technique would be to further examine the effects of electrostatic contributions to the partitioning of species by increasing the valency of charge as well as the size of the charged compound. There are also

potential applications to study the diffusion of species into hydrogels under fluidic pressure as in a tissue chip format.[39] The methods developed herein may find applicability in research in those fields.

In the translational space, extracellular vesicles have gained prominence as a potential therapeutic as well as biomarker for a variety of diseases.[18] The results of this work suggest that the hydrogels may serve as viable surrogates to characterize the local deposition of enrichment of extracellular vesicles in the native microenvironment of a variety of pathologies and physiological processes.[40] Indeed, reports have emerged detailing the enrichment of specific subtypes of extracellular vesicles with the tumor stroma.[19] Furthermore, development of novel technologies enabling the characterization of secretions at the single cell level have reached a critical point and may usher in an era of secretome biology.[41] In that context, the methodology explored in this paper will be useful to future generations which seek to understand and isolate the effects of matrix properties on the cellular secretome.

4.5. References

1. Lue, P. Limitations of 2D Cell Culture.
2. Li, Y., Xiao, Y. & Liu, C. The Horizon of Materiobiology: A Perspective on Material-Guided Cell Behaviors and Tissue Engineering. *Chemical Reviews* **117**, 4376–4421 (2017).
3. Kotlarchyk, M. A., Botvinick, E. L. & Putnam, A. J. Characterization of hydrogel microstructure using laser tweezers particle tracking and confocal reflection imaging. *J Phys Condens Matter* **22**, 194121 (2010).
4. Reinhart, C. T. & Peppas, N. A. Solute diffusion in swollen membranes. Part II. Influence of crosslinking on diffusive properties. *J. Membr. Sci.* **18**, 227–239.

5. Modelling the endothelial blood-CNS barriers: a method for the production of robust in vitro models of the rat blood-brain barrier and blood-spinal cord barrier. *BMC Neuroscience* **14**, 59 (2013).

6. Axpe, E. *et al.* A Multiscale Model for Solute Diffusion in Hydrogels. *Macromolecules* **52**, 6889–6897 (2019).

7. Discher, D. E., Mooney, D. J. & Zandstra, P. W. Growth factors, matrices, and forces combine and control stem cells. *Science* vol. 324 1673–1677 (2009).

8. Spatially controlled simultaneous patterning of multiple growth factors in three-dimensional hydrogels. *Nature Materials* **10**, 799–806 (2011).

9. Liao, H. *et al.* Influence of hydrogel mechanical properties and mesh size on vocal fold fibroblast extracellular matrix production and phenotype. *Acta Biomaterialia* **4**, 1161–1171 (2008).

10. McKenna, M., Shackelford, D., Ferreira Pontes, H., Ball, B. & Nance, E. Multiple Particle Tracking Detects Changes in Brain Extracellular Matrix and Predicts Neurodevelopmental Age. *ACS Nano* **15**, 8559–8573 (2021).

11. Dong, P., Schott, B. J., Means, A. K. & Grunlan, M. A. Comb Architecture to Control the Selective Diffusivity of a Double Network Hydrogel. *ACS Applied Polymer Materials* **2**, 5269–5277 (2020).

12. Johansson, L., Elvingson, C. & Löfroth, J. E. Diffusion and Interaction in Gels and Solutions. 3. Theoretical Results on the Obstruction Effect. *Macromolecules* **24**, 6024–6029 (1991).

13. Vernerey, F. J., Lalitha Sridhar, S., Muralidharan, A. & Bryant, S. J. Mechanics of 3D Cell-Hydrogel Interactions: Experiments, Models, and Mechanisms. *Chemical Reviews* **121**, 11085–11148 (2021).

14. Skouri, R., Schosseler, F., Munch, J. P. & Candau, S. J. Swelling and Elastic Properties of Polyelectrolyte Gels. *Macromolecules* **28**, 197–210 (1995).

15. Sonker, M. *et al.* Review of Recent Advances and Their Improvement in the Effectiveness of Hydrogel-Based Targeted Drug Delivery: A Hope for Treating Cancer. *ACS Applied Bio Materials* **4**, 8080–8109 (2021).

16. Cukier, R. I. Diffusion of Brownian Spheres in Semidilute Polymer Solutions. *Macromolecules* **17**, 252–255 (1984).

17. Morad, G. & Moses, M. A. Brainwashed by extracellular vesicles: the role of extracellular vesicles in primary and metastatic brain tumour microenvironment. *Journal of Extracellular Vesicles* vol. 8 (2019).

18. Raposo, G. & Stoorvogel, W. Extracellular vesicles: Exosomes, microvesicles, and friends. *Journal of Cell Biology* vol. 200 373–383 (2013).

19. Yekula, A. *et al.* Extracellular Vesicles in Glioblastoma Tumor Microenvironment. *Frontiers in Immunology* vol. 10 (2020).

20. Hickey, A. S. & Peppas, N. A. Mesh size and diffusive characteristics of semicrystalline poly(vinyl alcohol) membranes prepared by freezing/thawing techniques. *Journal of Membrane Science* **107**, 229–237 (1995).

21. Reitan, N. K., Juthajan, A., Lindmo, T. & de Lange Davies, C. Macromolecular diffusion in the extracellular matrix measured by fluorescence correlation spectroscopy. *Journal of Biomedical Optics* **13**, 054040 (2008).

22. Turco, G. *et al.* Mechanical spectroscopy and relaxometry on alginate hydrogels: A comparative analysis for structural characterization and network mesh size determination. *Biomacromolecules* **12**, 1272–1282 (2011).

23. Sheng, F. & Yi, J. Characterization of Dextran using Light Scattering Techniques. 1–5 (2015).

24. Wang, J. & Wang, J. Molecular weight characterization of high molecular weight dextran with multiangle light scattering in on-line and off-line mode. *Biopolymers* **103**, 387–392 (2015).

25. Ehsanipour, A. *et al.* Injectable, macroporous scaffolds for delivery of therapeutic genes to the injured spinal cord. *APL Bioengineering* **5**, 16104 (2021).

26. Xiao, W. *et al.* Brain-mimetic 3D culture platforms allow investigation of cooperative effects of extracellular matrix features on therapeutic resistance in glioblastoma. *Cancer Research* **78**, 1358–1370 (2018).

27. Xiao, W. *et al.* Bioengineered scaffolds for 3D culture demonstrate extracellular matrix-mediated mechanisms of chemotherapy resistance in glioblastoma. *Matrix Biology* **85–86**, 128–146 (2020).

28. Ghochani, Y. *et al.* Generation of a molecular interactome of the glioblastoma perivascular niche reveals Integrin Binding Sialoprotein as a key mediator of tumor cell migration. *bioRxiv* 2021.10.01.462643 (2021) doi:10.1101/2021.10.01.462643.

29. Henke, M., Brandl, F., Goepferich, A. M. & Tessmar, J. K. Size-dependent release of fluorescent macromolecules and nanoparticles from radically cross-linked hydrogels. *European Journal of Pharmaceutics and Biopharmaceutics* **74**, 184–192 (2010).

30. Richbourg, N. R. *et al.* Precise control of synthetic hydrogel network structure via linear, independent synthesis-swelling relationships. *Science Advances* **7**, eabe3245 (2021).

31. Richbourg, N. R. & Peppas, N. A. High-Throughput FRAP Analysis of Solute Diffusion in Hydrogels. *Macromolecules* **54**, 10477–10486 (2021).

32. Chmelík, J., Chmelíková, J. & Novotny, M. v. Characterization of dextrans by size-exclusion chromatography on unmodified silica gel columns, with light-scattering detection, and capillary electrophoresis with laser-induced fluorescence detection. *Journal of Chromatography A* **790**, 93–100 (1997).

33. Wang, J. & Wang, J. Molecular weight characterization of high molecular weight dextran with multiangle light scattering in on-line and off-line mode. *Biopolymers* **103**, 387–392 (2015).

34. Specific refractive index increments of dextran fractions of different molecular weights. https://onlinelibrary.wiley.com/doi/epdf/10.1002/macp.1978.021790523.

35. Dalal, I. S., Hsieh, C. C., Albaugh, A. & Larson, R. G. Effects of excluded volume and hydrodynamic interactions on the behavior of isolated bead-rod polymer chains in shearing flow. *AIChE Journal* **60**, 1400–1412 (2014).

36. Some, D., Amartely, H., Tsadok, A. & Lebendiker, M. Characterization of Proteins by Size-Exclusion Chromatography Coupled to Multi-Angle Light Scattering (SEC-MALS). *JoVE (Journal of Visualized Experiments)* **2019**, e59615 (2019).

37. Falke, S. & Betzel, C. Dynamic Light Scattering (DLS). 173–193 (2019) doi:10.1007/978-3-030-28247-9_6.

38. Stetefeld, J., McKenna, S. A. & Patel, T. R. Dynamic light scattering: a practical guide and applications in biomedical sciences. *Biophysical Reviews* **8**, 409–427 (2016).

39. Akay, M. *et al.* Drug Screening of Human GBM Spheroids in Brain Cancer Chip. *Scientific Reports* **8**, 15423 (2018).

40. al Halawani, A., Mithieux, S. M., Yeo, G. C., Hosseini-Beheshti, E. & Weiss, A. S. Extracellular Vesicles: Interplay with the Extracellular Matrix and Modulated Cell Responses. *Int J Mol Sci* **23**, (2022).

41. de Rutte, J., Dimatteo, R., Zhu, S., Archang, M. M. & di Carlo, D. Sorting single-cell microcarriers using commercial flow cytometers. *SLAS Technology* **27**, 150–159 (2022).

Chapter 5. Conclusion

The overwhelming lethality of Glioblastoma (GBM) has spurred many efforts to develop novel therapies to improve patient outcomes. The large number of failed clinical trials for targeted and mechanism specific therapies urge the development of better preclinical models which can more faithfully recapitulate GBM tumor biology. Previous work has revealed the capacity for hyaluronic acid which is upregulated in the GBM tumor microenvironment (TME) to provide crucial signaling and pathway activation which increase the drug resistance and ultimate lethality of GBM. These signaling pathways are conserved in *ex vivo* models of GBM as demonstrated through studies utilizing patient derived GBM cells cultured in HA-based hydrogels. In most formulations, the manufacture of these cell-laden hydrogel constructs is artisanal in nature and require considerable skill and finesse to fabricate which has limited their inherent utilization in high throughput assays.

The objective of this dissertation has been the development of methods to adapt hydrogel augmented cultures to high-throughput screening assays. This was demonstrated and reduced to practice in both 2- and 3-dimensional formats. Additionally, for greater physiological relevance phenotypic screening approaches have been developed to accommodate more biologically complex readouts such as cytoskeletal remodeling, cell cycling and spheroid formation assays in chapters 2 and 3. Future directions for this portion of the dissertation would be partnering with entities in possession of chemical libraries and performing compound screens to identify novel therapeutics for further development. Beyond exploring the effects of compounds or drugs on the phenotypes of GBM cultures, this dissertation explores methods for the screening of physical

matrix components. Indeed, the rich diversity of extracellular matrix (ECM) proteins and other macromolecules in the GBM TME also varies considerably between patients.

Thus, applications for personalized medicine to empirically identify patient-derived cell line-specific responses to therapeutics were further explored in chapter 3. As discussed in chapter 3, the interpatient heterogeneity displayed by GBM is staggering and it is likely that the relative inefficacy of modern treatments for GBM stem from a failure of tailor-made therapies. A critical strategy moving forward in GBM therapies will be leveraging technologies that can provide insight and predictions of patient-specific responses. As such, the methods described in chapter 3 will undoubtedly prove useful to help relate microenvironment features to drug resistance. Indeed, advancements in spatial sequencing will allow for increased correlation of gene expression to ECM features in patient tumors, enabling the identification of drug resistant subpopulations in patient tumors. Furthermore, improvements in the proteomics space Specifically in the mass spectrometry and artificial intelligence technologies will simultaneously aid in the profiling of ECM composition of patient tumors. The molecular and proteomic signatures obtained by these methods can be incorporated into the hydrogel-based screening platform for next generation patient-specific profiling.

Over the past 10 years a boom in the development of immunotherapeutic modalities for GBM has occurred with applications of oncolytic virotherapy, chimeric antigen receptor (CAR), and checkpoint blockers seeing testing in clinical trials.[1–4] In particular CAR-T cell therapies have seen encouraging results in liquid tumors, but progress in solid tumors, like GBM, has been discouragingly slow.[2] This lack of progress has often been attributed to the immunosuppressive microenvironment of “cold” tumors as well and the physical tumor stroma, which inhibit

penetration of these therapeutics to target cells. Novel methods to characterize hydrogel environments based on solute penetration were described in chapter 4 of this dissertation. This was done systematically by using tissue engineering principles to modulate the physical characteristics of hydrogels. The measurements described in chapter 4 suggest that successful deployment of an immunotherapeutic to target GBM tumors will require strategies to overcome the potential barrier presented by the tumor stroma. All in all, the work in this dissertation seeks to improve the process of developing therapeutics for GBM by leveraging tissue engineering principles to develop preclinical models that more faithfully recapitulate GBM *in vitro* thereby allowing for more rigorous testing of potential therapeutics.

5.1. References

1. Huang, J. *et al.* Immune checkpoint in glioblastoma: Promising and challenging. *Frontiers in Pharmacology* (2017) doi:10.3389/fphar.2017.00242.
2. de Bousser, E., Callewaert, N. & Festjens, N. T Cell Engaging Immunotherapies, Highlighting Chimeric Antigen Receptor (CAR) T Cell Therapy. *Cancers (Basel)* **13**, (2021).
3. Kaufman, H. L., Kohlhapp, F. J. & Zloza, A. Oncolytic viruses: a new class of immunotherapy drugs. *Nat Rev Drug Discov* **14**, 642–662 (2015).
4. Advances in Experimental Targeted Therapy and Immunotherapy for Patients with Glioblastoma Multiforme. *Anticancer Research* **37**, 21–33 (2017).